Fall 2019

Start-up Power Requirements of Ammonia Filled Aerospace Thermosyphon Heat Pipes

Eric Chu
San Jose State University

START-UP POWER REQUIREMENTS OF AMMONIA FILLED AEROSPACE THERMOSYPHON HEAT PIPES

A Thesis

Presented to

The Faculty of the Department of Mechanical Engineering

San José State University

In Partial Fulfillment

of the Requirement for the Degree

Master of Science

by

Eric Chu

December 2019

The Designated Thesis Committee Approves the Thesis Titled

START-UP POWER REQUIREMENTS
OF AMMONIA FILLED AEROSPACE
THERMOSYPHON HEAT PIPES

by

Eric Chu

APPROVED FOR THE DEPARTMENT OF MECHANICAL ENGINEERING

SAN JOSÉ STATE UNIVERSITY

December 2019

Nicole Okamoto, Ph.D.	Department of Mechanical Engineering
Syed Zaidi, Ph.D.	Department of Mechanical Engineering
Ernie Thurlow, Ph.D.	Department of Mechanical Engineering

ABSTRACT

START-UP POWER REQUIREMENTS
OF AMMONIA FILLED AEROSPACE
THERMOSYPHON HEAT PIPES

by Eric Chu

Boiling and condensing of internal working fluids are essential heat transfer concepts which heat pipe technology relies on for transporting a large amount of heat between two distanced points effectively. Tilt angle and working fluid saturation temperature have a direct impact on how well the evaporator is flooded. This paper focuses on how the tilt angle and the working fluid saturation temperature affect the start-up heat input requirements for an S shaped axial grooved ammonia thermosyphon heat pipe. A series of experiments was performed by supplying and extracting heat to the evaporator and condenser of the thermosyphon heat pipe. Temperature of the evaporator and condenser was monitored to capture start-up behavior upon heat input. The evaporator temperature was found to be slightly elevated before the internal working fluid begins to boil. It decreased once boiling starts and initiates the thermosyphon process. The test results showed that the evaporator start-up temperature difference was found to be higher as fluid saturation temperature increases, and becomes lower as the fluid saturation temperature decreases. The start-up heat input requirement to initiate start-up in the evaporator was determined to be constant throughout the range of tilt angles and saturation temperatures.

ACKNOWLEDGMENTS

I would like to express my deep gratitude to the committee members, Dr. Okamoto, Dr. Zaidi, and Dr. Thurlow for the valuable guidance they have given me, guiding the project to the finish line. Special thanks to Mr. Randy Pon, Dr. Okamoto, and San Jose State University for the opportunity to work on this project. Finally, I would like to thank my wife and my family for the continuous support they have provided me throughout the course of this project.

TABLE OF CONTENTS

LIST OF TABLES

LIST OF FIGURES

Nomenclature

Symbol	Description
A_{flange}	Heat pipe flange heat transfer surface area
C_{pl}	Specific heat of liquid
C_{sf}	Experimental surface-fluid constant
g	Gravitational Acceleration
h_{fg}	Enthalpy of Vaporization
k	Thermal conductivity
$L_{heat\ pipe}$	Heat pipe Length
P_{input}	Electrical input power
Pr_l	Prandtl Number of liquid
$\dot{q}_{nucleate}$	Nucleate boiling heat flux
$\dot{Q}_{input}$	Input Power
$\dot{Q}_{\substack{loss \\ adiabatic}}$	Adiabatic section heat loss
$\dot{Q}_{\substack{loss \\ evaporator}}$	Evaporator heat loss
R_{loss}	Heat loss thermal resistance
$T_{condenser}$	Condenser temperature
$T_{evaporator}$	Evaporator temperature
T_{excess}	Excess temperature
T_s	Temperature of heated surface
T_{sat}	Saturation temperature of fluid
v_{avg}	Average specific volume
v_{liquid}	Liquid specific volume
v_{vapor}	Vapor specific volume
x	Quality

Greek

Symbol	Description
μ_l	Viscosity of liquid
ρ_l	Density of liquid
ρ_v	Density of vapor
σ	Surface tension of liquid-vapor interface

1.0 Introduction

Boiling and condensing of working fluids are essential heat transfer concepts which heat pipe technology relies on for transporting a large amount of heat between two distanced points effectively. Gravitational force plays a major role in the heat transfer limitation and characteristics of heat pipes that are designed differently. This paper will focus on how the tilt angle and initial temperature affect the start-up heat input requirements for an "S shaped" axial grooved thermosyphon heat pipe. The start-up heat input requirements have been analyzed at tilt angles of 90º to 0º, from vertical to horizontal operation in increments of 10° at a range of initial saturation temperature from 20°C to 60°C in increments of 10°C.

Heat pipes are widely used in various applications including electronic cooling, aerospace, power generation cycles, heat recovery in HVAC systems, and in many other fields. They are designed differently for specific applications. Heat pipes are fixed volume, two-phase heat transfer devices that are able to transport heat over a distance effectively with a small temperature gradient. A heat pipe has a few different major parts, the evaporator, the condenser, and the adiabatic section. The internal working fluid absorbs heat and transforms into a vapor state internally at the evaporator section of a heat pipe. Then the vapor travels through the adiabatic section to the condenser section of the heat pipe due to the vapor pressure. The adiabatic section connects the evaporator and the condenser section of the heat pipe with no significant amount of heat transfer added to the overall system. The condenser section removes heat, which condenses the vapor that traveled from the evaporator section and sends the saturated liquid back to the

evaporator through the adiabatic section. Figure 1 shows a typical heat pipe's construction and operation.

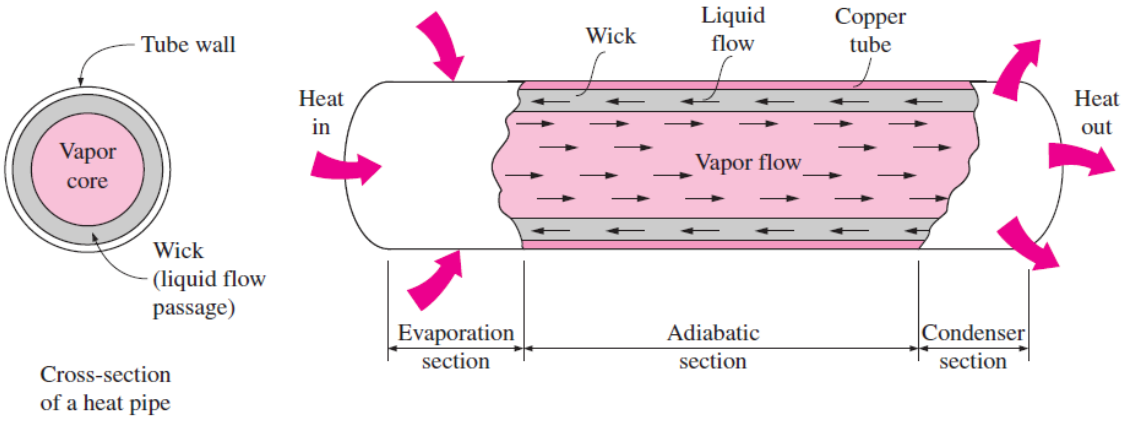

Figure 1. Schematic and operation of a heat pipe [1].

An S shaped axial grooved thermosyphon heat pipe is analyzed in this paper. This specific heat pipe belongs to a network of heat pipes used on a telecommunication satellite to help reject heat and maintain operational temperature for the electronics of the satellite's payload. Figure 2 and Figure 3 show the picture and the approximate location of the S shaped heat pipe on a satellite.

Figure 2. S shaped thermosyphon heat pipes.

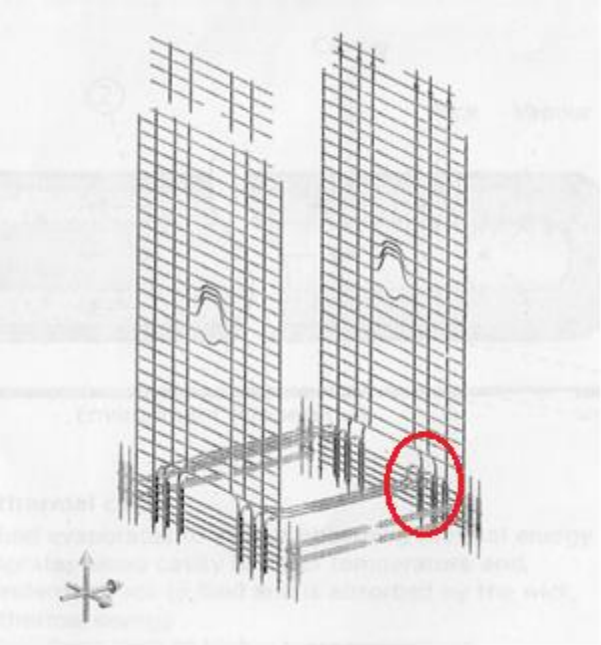

Figure 3. Satellite heat pipe network [4].

This S shaped thermosyphon heat pipe doesn't have an internal wick structure to assist the condensed fluid to return from the condenser to the evaporator. It is designed to operate in outer space in microgravity. Instead of having an internal wick structure, it has internal axial grooves as pictured in a cutaway section of the evaporator in Figure 4. This S shaped heat pipe is filled with 39.4 grams of ammonia in a fixed internal volume of 0.000192 m^3 with 25 evenly spaced internal axial grooves, which formed a 0.398 inch vapor core diameter and a 0.524 inch inner tube diameter. This heat pipe utilizes ammonia as its internal working fluid. The saturated liquid occupies and travels in between the grooves throughout the heat pipe while the saturated vapor travels in the center vapor core between the evaporator and condenser. Capillary action helps the saturated liquid to evenly distribute in between the axial grooves.

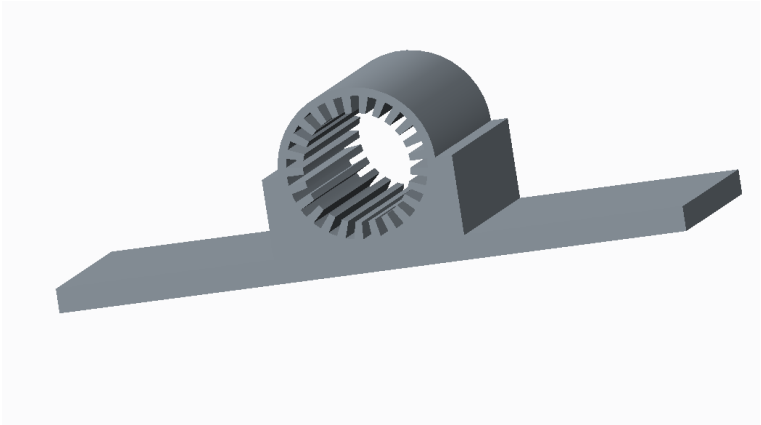

Figure 4. Evaporator cross-sectional view.

1.1 Literature Review

Previous studies analyzed the start-up characteristics of heat pipes. In a study conducted out by Qu, Wu, and Cheng [2], the start-up characteristics of three horizontal micro pulsating looped heat pipes were analyzed in 2012. The heat pipes were charged with several different types of working fluids for comparison. Heat was supplied at the evaporator and retrieved at the condenser of the micro pulsating heat pipe. The focus of this study was to analyze and determine the compatibility and start-up behavior of several different working fluids in the heat pipes. The data clearly show a significant change in temperatures at the evaporator and the condenser upon start-up. Figure 5 and Figure 6 show the start-up thermal test setup and temperature plots of the heat pipes over time.

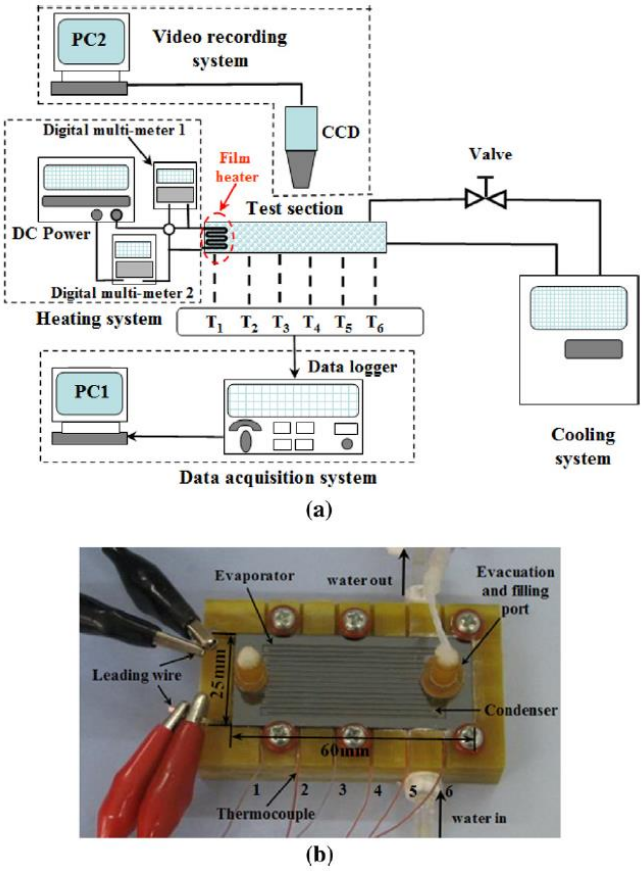

Figure 5. Heat pipe test setup [2].

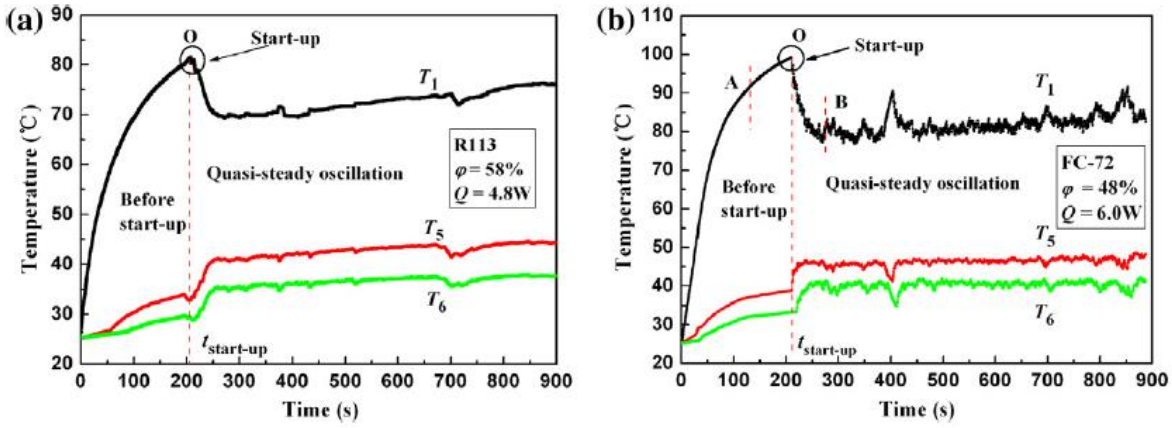

Figure 6. Heat pipe start-up characteristics [2].

There is a noticeable decrease in temperature at the evaporator, T_1, and increase in temperature at the condenser, T_5 and T_6. Temperatures were taken with thermocouples instrumented onto the body of the heat pipe, and heat was applied at the evaporator with a DC film heater while heat was extracted with supplied water at the condenser in this study.

In another study carried out by Mameli, Catarsi, Mangini, Pietrasanta, Miche, Marengo, Marco, Filippeschi [3], the start-up characteristics of a loop thermosyphon were analyzed in 2019. The study was conducted in the presence of microgravity during parabolic flights. The test data show a significant temperature decrease at the evaporator, and a noticeable temperature increase at the condenser upon start-up at 1070 seconds. Figure 7 and Figure 8 show test data plots over time and the test setup.

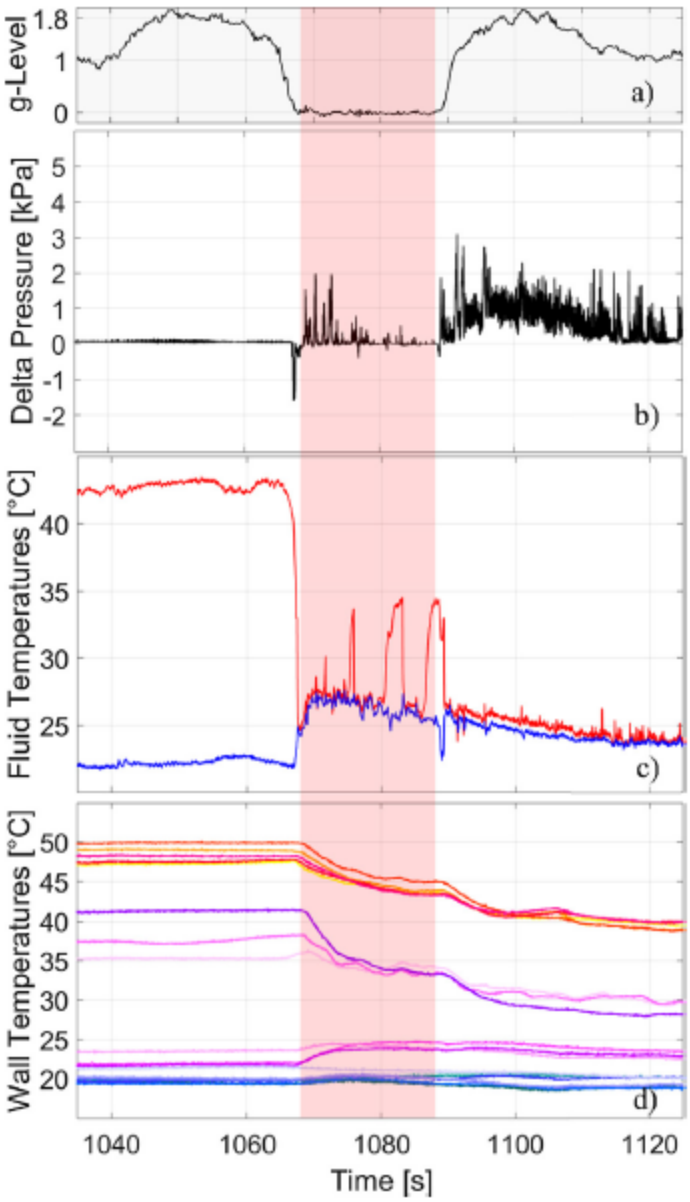

Figure 7. Loop thermosyphon start-up data [3].

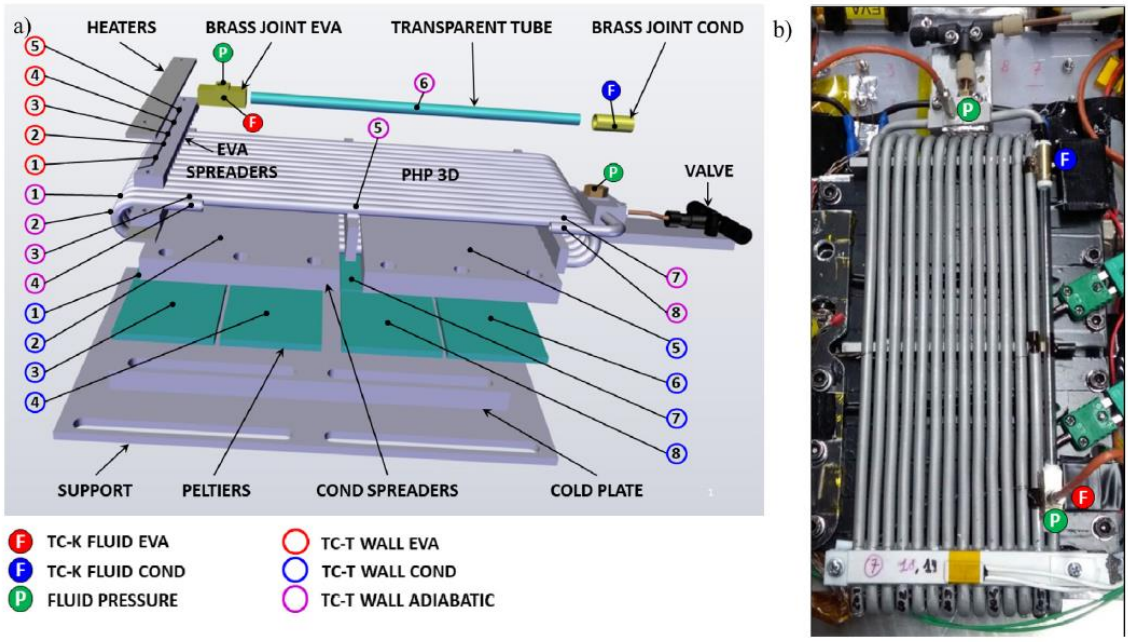

Figure 8. Micro gravity loop thermosyphon setup [3].

1.2 Objectives

The minimum start-up heat input requirements will be analyzed on the "S shaped" thermosyphon axial grooved heat pipe from tilt angles of 0-90° in increments of 10° at initial saturation temperatures of 20-60°C in 10°C increments. Start-up characteristics of the heat pipe will be evaluated to determine the amount of heat required to initiate the thermosyphon process inside the heat pipe.

2.0 Methodology

To provide tilt angle, heat supply, heat extraction, and temperature acquisitions to analyze the start-up characteristics of the S shaped axial grooved heat pipe, a heat pipe testing apparatus was designed and constructed from 2011 to 2012 at San Jose State University with financial support from Space System Loral. The testing apparatus was designed to accept and provide heat supply, heat extraction, tilt angle, and temperature

acquisitions for “S shaped” heat pipes. The testing apparatus consists of an enclosure made of aluminum extrusion fitted with linear bearings. It provides tilt angles to the heat pipe assemblies. Electric resistance heaters provide heat to the evaporator while a water chiller provides chilled water to extract heat from the condenser. Figure 9 shows a picture of the heat pipe testing apparatus with the insulated heat pipe installed at a tilt angle.

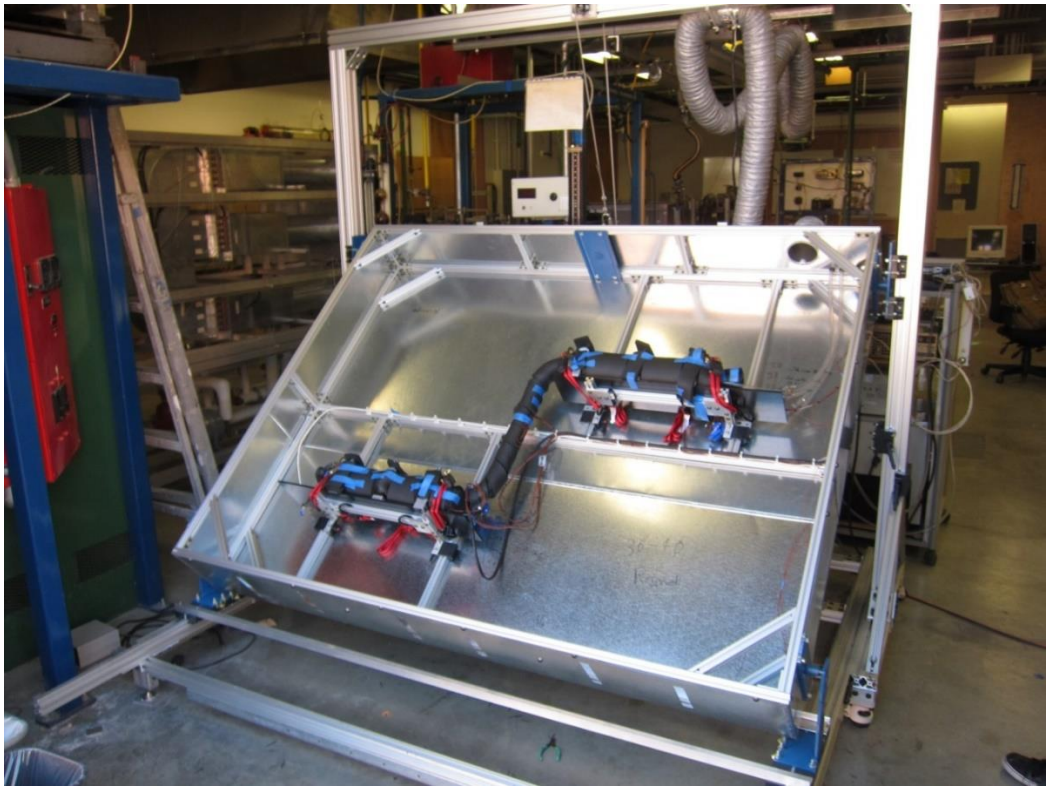

Figure 9. Heat pipe testing apparatus.

The heat pipe was tested with a series of tilt angles and saturation temperatures to analyze the effect of tilt angle and saturation temperatures on minimum start-up power. A series of tests with tilt angles of 0-90° in increments of 10° at initial starting temperatures of 20-60°C were conducted. The entire heat pipe assembly was maintained

at a constant temperature by supplying temperature-controlled chilled water to the condenser before each test. The heat pipe assembly had to reach thermal equilibrium before each test. Boiling and condensation are not expected to happen inside the heat pipe before heat was being input at the evaporator. A constant heat load was supplied to the evaporator while temperature measurements were taken throughout the body of the heat pipe to monitor the start-up characteristics of the heat pipe. Figure 10 shows the experimental setup. Heat was supplied to the evaporator with electrical heating elements and a copper block was utilized as a heat spreader to minimize temperature differences across the evaporator. Heat was extracted at the condenser, which is attached to a cold plate heat exchanger supplied with running chilled water.

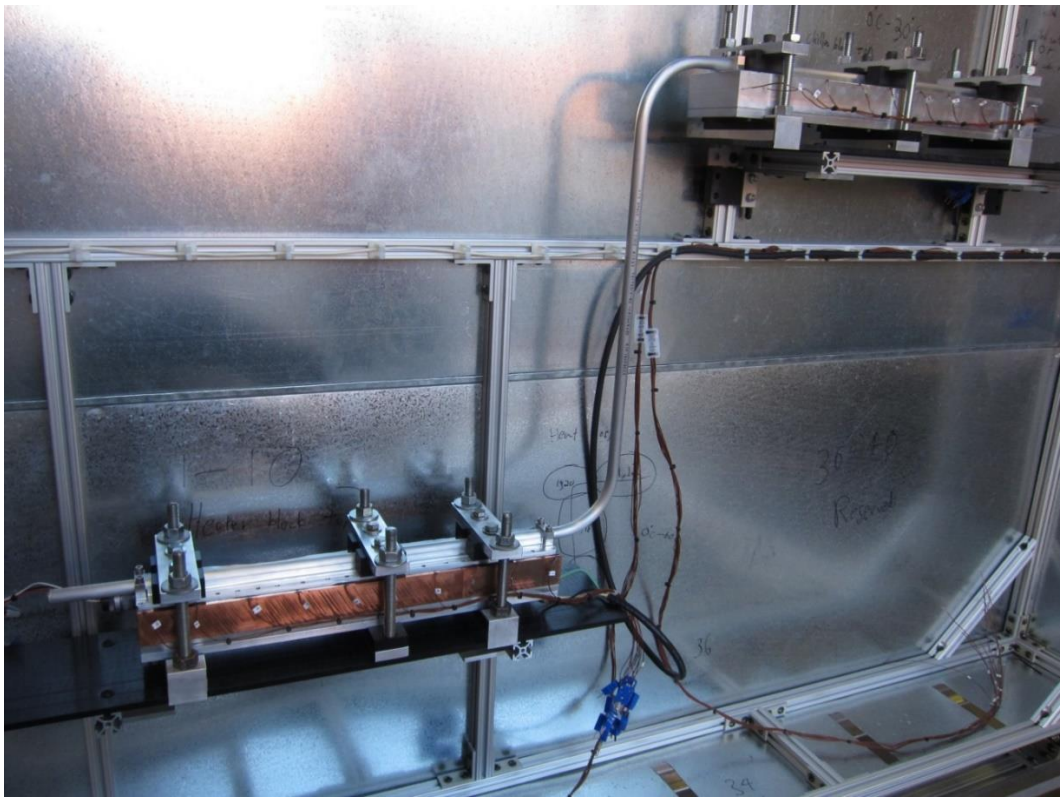

Figure 10. Experiment setup.

2.1 Analytical Work

2.1.1 Saturated Liquid vs. Vapor Ratio

The amount of saturated fluid collected at the evaporator has direct impacts on the minimum start-up heat input requirement of the heat pipe. Since heat pipes are closed, fixed volume, two-phase heat transfer devices, the ratio of saturated liquid to vapor is directly related to the internal fluid saturated temperature, which is the initial storage temperature of the heat pipe. The intended design of axial grooved thermosyphon heat pipes is to allow saturated working fluid to occupy between the axial grooves along with saturated vapor occupying the vapor core during normal operation with in microgravity in outer space. Orientation of the heat pipe does not affect the boiling performance of the working fluid in outer space without the presence of gravity; the boiling surfaces in between the grooves at the evaporator section would ideally always be wetted with saturated working fluid, ready to be boiled and transformed into vapor state in outer space. Figure 11 illustrates the location of the saturated fluid without the presence of gravity, shown in blue.

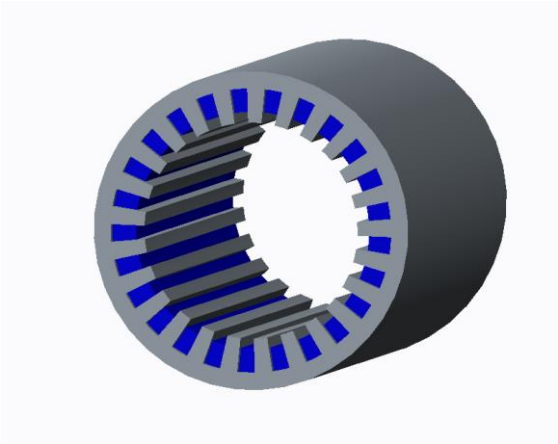

Figure 11. Saturated liquid filled axial grooves.

The working fluid behaves differently on ground level with the presence of gravity. This axial grooved thermosyphon heat pipe requires the evaporator be oriented lower than the condenser for the saturated liquid to drain properly from the condenser back to the evaporator with the presence of gravity. The saturated liquid floods the entire evaporator section of the heat pipe including the vapor core due to the density difference between the vapor and liquid state of the working fluid. The boiling surface at the evaporator is affected depending on the total mass of the working fluid, the saturation temperature of the working fluid, and the tilt angle between the evaporator and condenser. If the evaporator is oriented higher than the condenser, the saturated liquid will not be able to return from condenser to evaporator properly due to gravity. It will have to rely on the combination of capillary action and axial groove geometry to travel against gravity. Figure 12 shows the fluid level of the cross-sectioned section of the heat pipe highlighted in green at 20°C with 39.4 grams of working fluid charge.

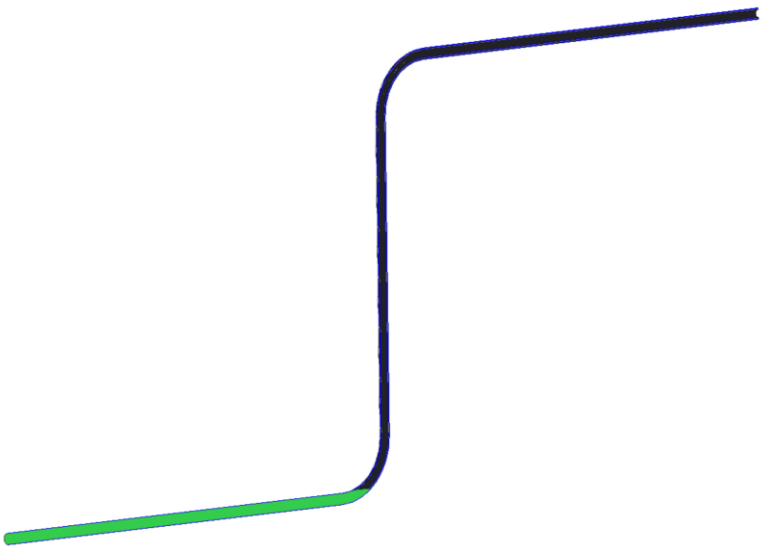

Figure 12. Cross-sectioned view of heat pipe.

The saturation pressure of the working fluid is directly proportional to the operating temperature of the heat pipe. Since the heat pipe is a closed system two-phase thermodynamic heat transfer device, the internal fluid pressure is equal to the saturation pressure of the working fluid. Ammonia has a maximum critical pressure at 11280 kPa at 132.4°C. Besides the high working pressure near the critical temperature, the enthalpy of vaporization of a working fluid becomes smaller as it approaches its critical temperature; therefore, ammonia heat pipes should not operate close to this temperature range. Figure 13 shows the saturation pressure and temperature relationship over ammonia's operating temperature range.

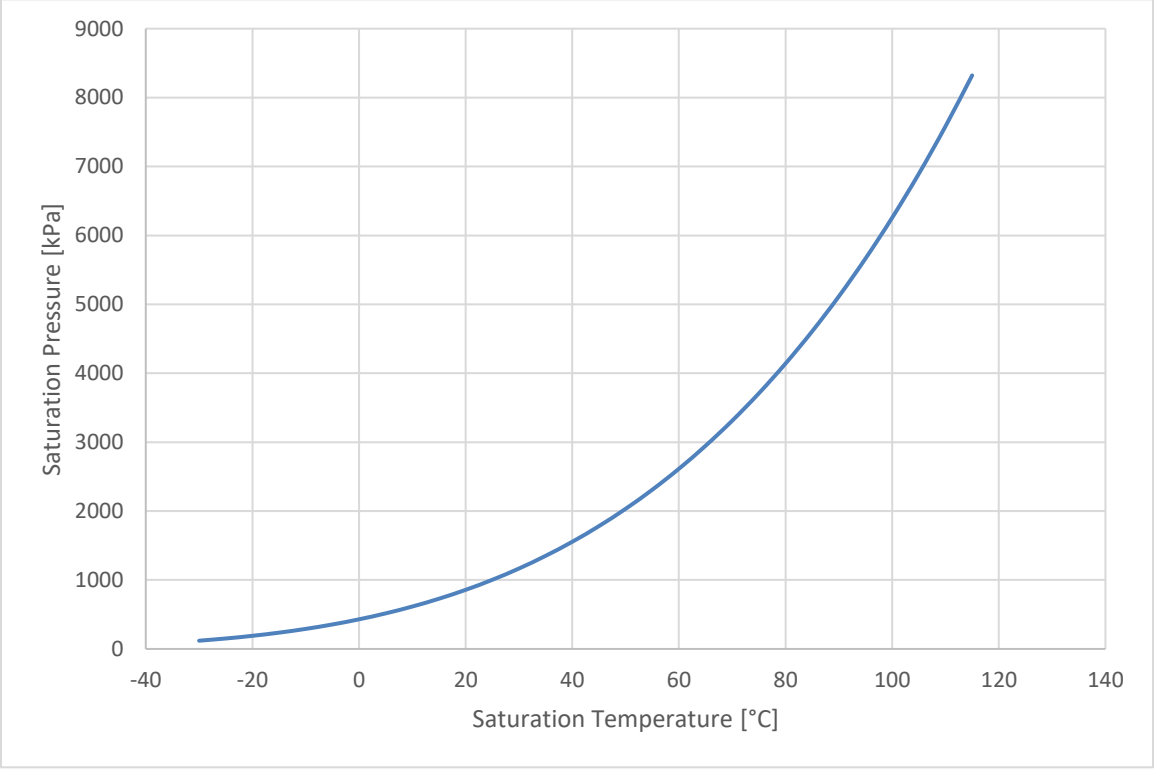

Figure 13. Ammonia NH3 saturation pressure vs. temperature chart [8].

Liquid and vapor volume fraction of the heat pipe's working fluid was analyzed to understand how the internal boiling surface area of the heat pipe evaporator can be affected by the saturation temperature of the working fluid and tilt angle of the heat pipe. For a working fluid contained in a fixed volume container, its fluids properties are dependent on temperature and pressure. The saturated vapor and liquid volumetric ratios can be calculated with a known volume, temperature, and mass of the working fluid. Equation 1 to Equation 6 analyze the quality, x, of the saturated working fluid contained in a fixed volume by utilizing the specific volumes of the saturated liquid and vapor.

$$v_{avg} = \frac{Volume_{heat\ pipe}}{Mass_{Ammonia\ Charge}} \tag{1}$$

$$x = \frac{v_{avg} - v_{liquid}}{v_{vapor} - v_{liquid}} \tag{2}$$

$$Volume_{liquid} = [1 - x](Mass_{Ammonia\ Charge})(v_{liquid}) \tag{3}$$

$$Volume_{vapor} = [x](Mass_{Ammonia\ Charge})(v_{vapor}) \tag{4}$$

$$Liquid\ Volume\ Fraction = \frac{Volume_{liquid}}{Volume_{heat\ pipe}} \tag{5}$$

$$Vapor\ \ Volume\ Fraction = \frac{Volume_{vapor}}{Volume_{heat\ pipe}} \tag{6}$$

The fluid properties used to determine the quality of the saturated fluid vary over the operating temperature range of the working fluid. The quality, x, defined in Equation 2 increases as temperature increases. As a result, the ratio of saturated vapor inside the heat pipe increases along with temperature. However, the specific volume of the saturated vapor decreases as temperature rises while the specific volume of the saturated liquid increases along with temperature. Therefore, the saturated liquid occupies a larger volume inside the heat pipe as temperature increases. Table 1 compares the vapor volume and liquid volume over a wide range of operating temperatures. Figure 14 and Figure 15 show how the vapor volume and liquid volume of the working fluid inside the heat pipe change over a wide range of operating temperatures.

Table 1. Vapor and Liquid Volume Ratio vs. Temperature Chart

Temperature [°C]	Vapor Volume [%]	Liquid Volume [%]
-70	71.7%	28.3%
-60	71.3%	28.7%
-50	70.9%	29.1%
-40	70.4%	29.6%
-30	69.9%	30.1%
-20	69.4%	30.6%
-10	68.8%	31.2%
0	68.3%	31.7%
10	67.7%	32.3%
20	67.2%	32.8%
30	66.6%	33.4%
40	66.0%	34.0%
50	65.4%	34.6%
60	64.9%	35.1%
70	64.3%	35.7%
80	63.7%	36.3%
90	63.2%	36.8%
100	62.8%	37.2%
110	62.7%	37.3%
120	63.3%	36.7%
130	69.0%	31.0%

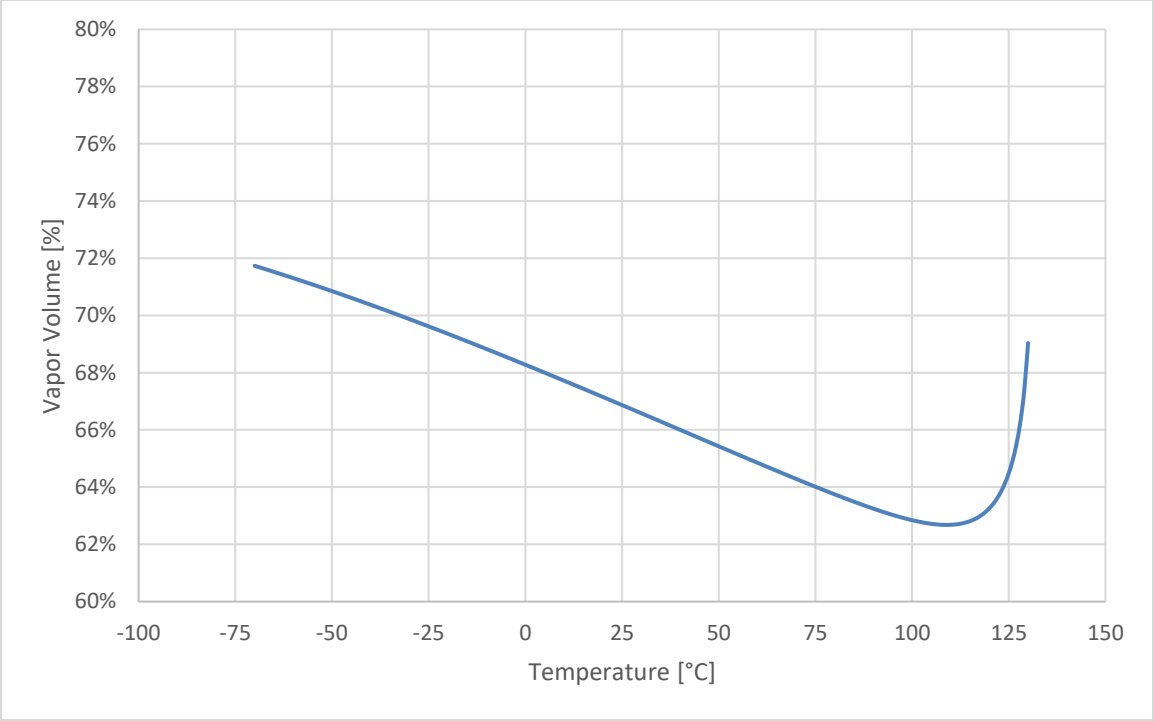

Figure 14. Saturated vapor volume ratio vs. temperature plot.

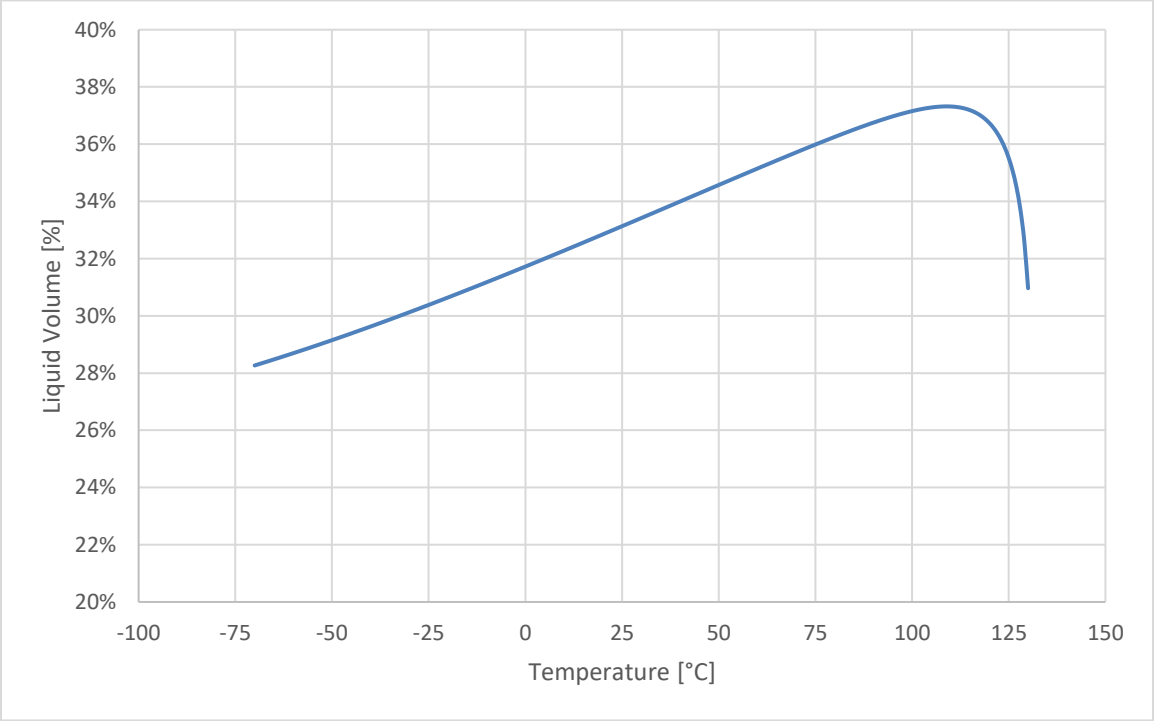

Figure 15. Saturated liquid volume ratio vs. temperature plot.

The wetted internal boiling surface area decreases as the saturated liquid volume decreases when the saturated temperature is lowered. The evaporator internal boiling surface area might not be fully flooded with saturated liquid at a low saturated temperature. Figure 16 shows how a partially flooded evaporator would look at low saturation temperatures and a fully flooded evaporator at a high saturation temperature.

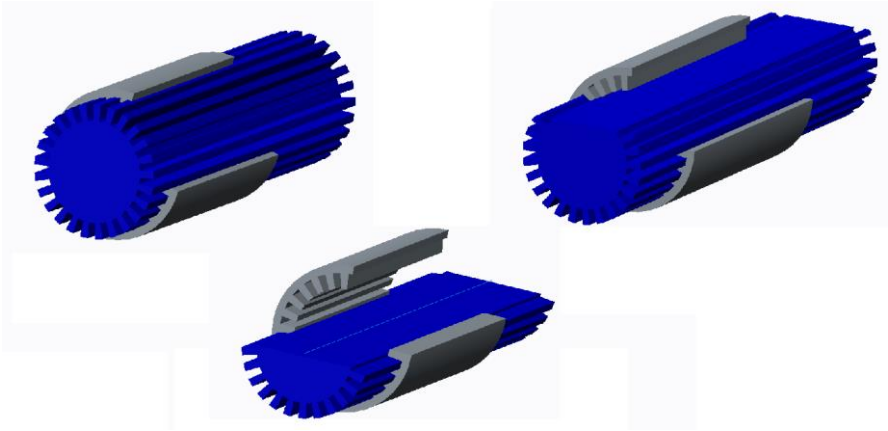

Figure 16. Partially flooded evaporator cutaway sections.

Figure 17 depicts the saturated liquid level inside the evaporator over a wide range of saturation temperatures. The volume of saturated liquid inside the heat pipe was calculated using Equation 2 and Equation 3. The evaporator becomes less flooded as temperature decreases. The wetted boiling surface area decreases as the evaporator becomes less flooded. The highlighted yellow and green overlays represent saturated liquid contained inside the evaporator at a vertical 90° tilt angle orientation.

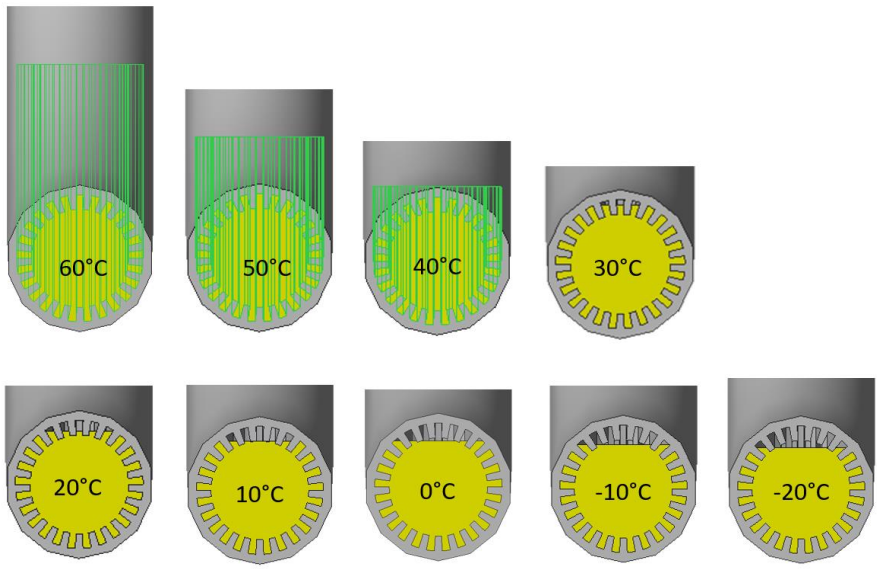

Figure 17. Saturation temperature effect on flooded evaporator section.

The saturated liquid and vapor ratios are also a function of the working fluid mass. At a constant pressure, the saturated liquid level inside the heat pipe varies depending on the total mass of the working fluid contained in the fixed volume which will affect how well the evaporator's boiling surface area is flooded.

Table 2 shows the relationship of saturated liquid and vapor's volumetric ratio with the total mass of the working fluid contained in a fixed volume at 20ºC. Figure 18 shows how the saturated liquid's volumetric ratio increases proportionally with the mass of working fluid.

Table 2. Fluid Volume Ratio vs. Ammonia Mass Chart

Mass [kg]	V % Vapor	V % Liquid
0.005	96.8%	3.2%
0.010	92.5%	7.5%
0.015	88.2%	11.8%
0.020	83.9%	16.1%
0.025	79.6%	20.4%
0.030	75.3%	24.7%
0.035	70.9%	29.1%
0.040	66.6%	33.4%
0.045	62.3%	37.7%
0.050	58.0%	42.0%
0.055	53.7%	46.3%
0.060	49.4%	50.6%
0.065	45.1%	54.9%
0.070	40.8%	59.2%
0.075	36.5%	63.5%
0.080	32.2%	67.8%
0.085	27.9%	72.1%
0.090	23.5%	76.5%
0.095	19.2%	80.8%
0.100	14.9%	85.1%

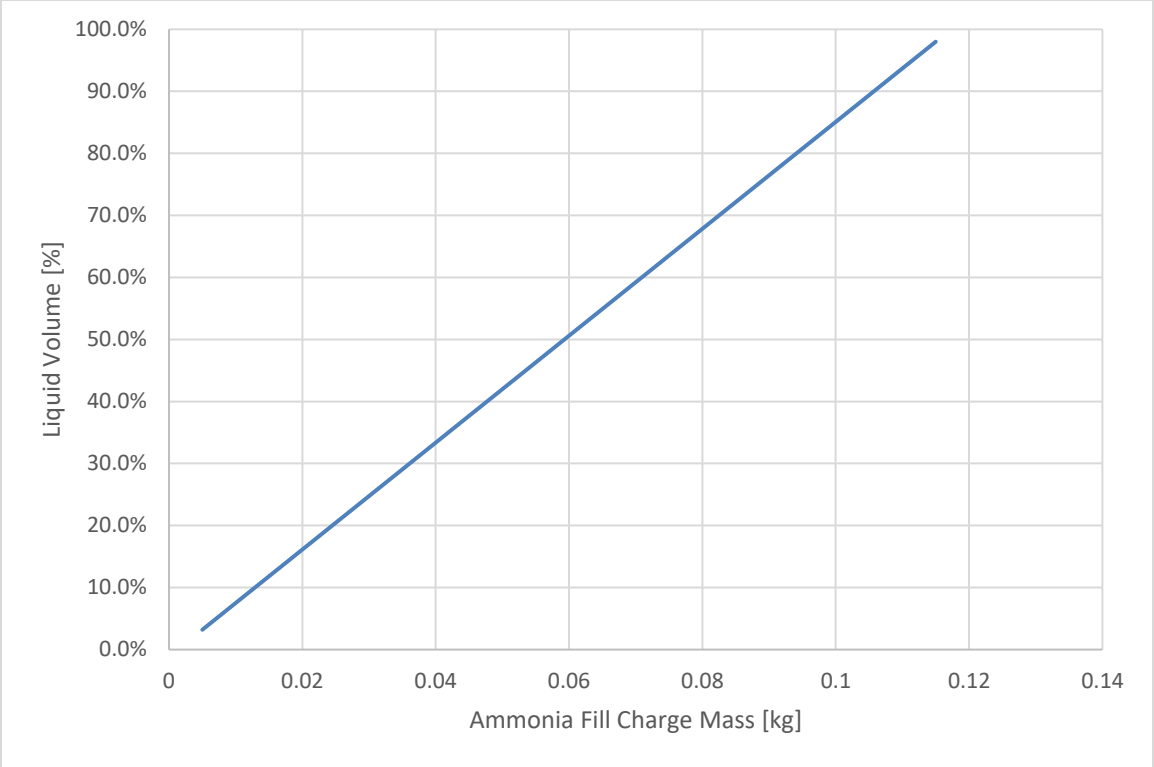

Figure 18. Liquid volume ratio vs. ammonia mass plot, 192cc, 20°C.

2.1.2 Flooded Evaporator Section vs. Tilt Angle

Tilt angle also affects how well the evaporator is flooded. As tilt angle decreases from the vertical 90° orientation, the working fluid inside the evaporator conforms with the contour of the internal axial grooves and begins to occupy the adiabatic section of the heat pipe. The evaporator becomes less flooded, and the saturated liquid spills out into the condenser section and occupies both evaporator and condenser section of the heat pipe as the tilt angle decreases to 0° horizontal orientation. Figure 19 depicts the tilt

angles' effect on the working fluid inside the heat pipe. The highlighted yellow and green sections represent saturated liquid.

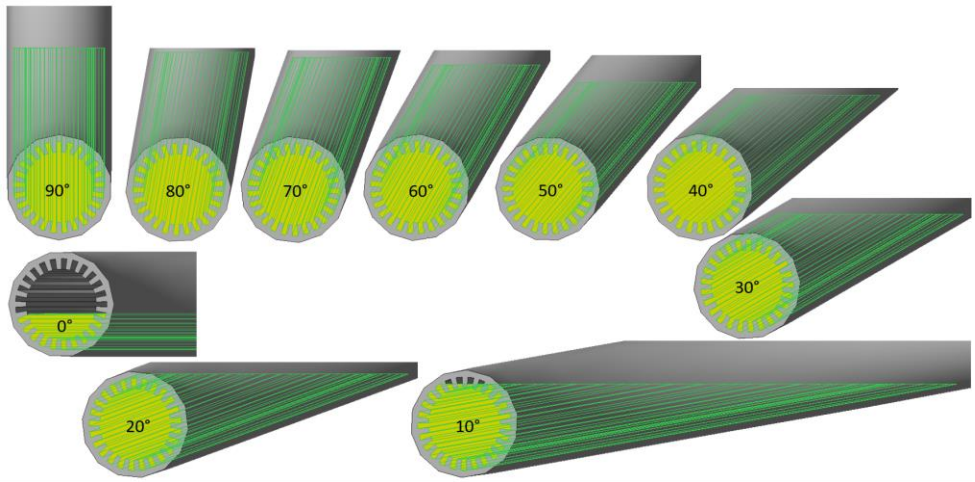

Figure 19. Tilt angle effect on flooded evaporator section.

2.2 Heat Pipe Thermal Conductivity Calculation

Thermal conductivity of the heat pipe is determined from the temperature difference, conduction distance, heat transfer surface area, and the rate of heat transfer between the evaporator and condenser. Equation 7 explains the relationship between the variables.

$$\frac{\dot{Q}_{input}}{A_{flange}} = -k\left[\frac{T_{evaporator} - T_{condenser}}{L_{heat\ pipe}}\right] \tag{7}$$

The amount of heat loss to the ambient environment between the evaporator and condenser needs to be subtracted from the overall rate of heat transfer for the thermal conductivity calculation to be accurate. Heat loss analysis of the heat pipe assembly will

be further discussed in Section 2.3 and Section 2.4. The conduction distance and heat transfer surface area used for thermal conductivity calculation is shown in Figure 20.

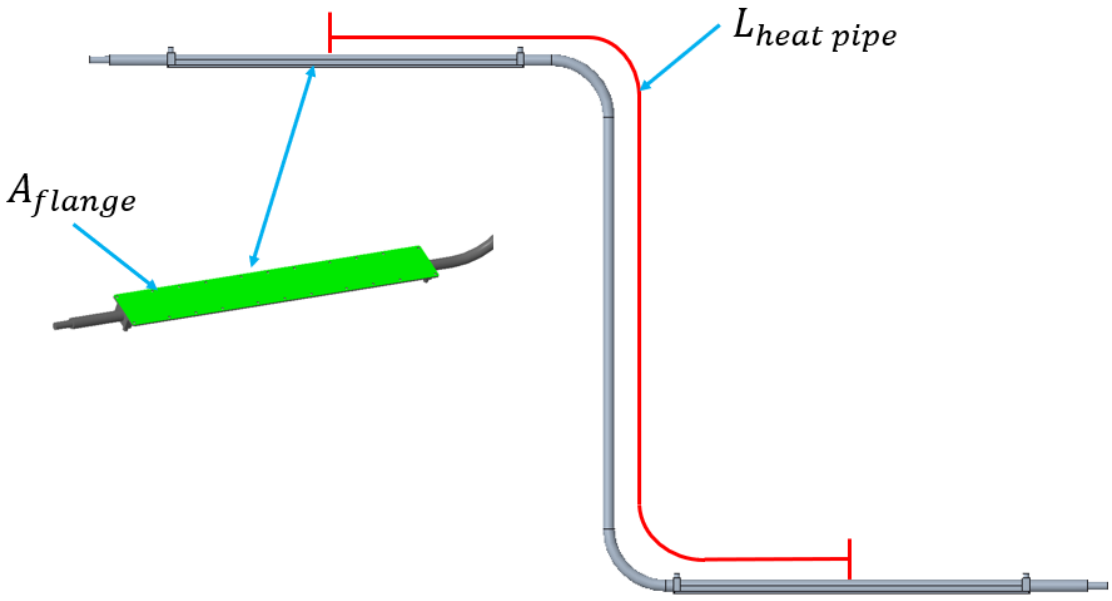

Figure 20. Length of heat pipe an flange area.

2.3 Heat Loss Calculation

Heat loss modeling is a critical part for an accurate thermal conductivity measurement of the heat pipe. Convection of heat from the heat pipe body and heat source is caused by temperature difference between heat pipe surface and room air. Calculation of the total amount of heat loss is required for an accurate heat pipe thermal conductivity determination. Insulation is applied to insulate over the surface of the heat pipe, chiller block, and heater block to minimize heat loss from convection. Air flows constantly inside the heat pipe enclosure box as a safety feature. The variation from the heat loss range is caused by the wide operating temperature range of the heat pipe from 20 °C to

60 °C while the ambient room temperature remains at 20°C. Heat loss calculation and measurements results are found in Sections 2.3.2 and 2.4.

2.3.1 Insulation

Insulation material needs to provide enough thermal resistance for proper insulation. Extruded polystyrene foam insulation sheets with a thermal conductivity value of 0.036W/mK was selected for constructing the insulation system. Figure 21 shows a sheet of extruded polystyrene foam.

Figure 21. Extruded polystyrene foam sheet.

An insulation system was designed with extrude polystyrene foam to insulate the entire heat pipe assembly. Multiple layers of insulation sheets were cut to size as shown in Figure 22.

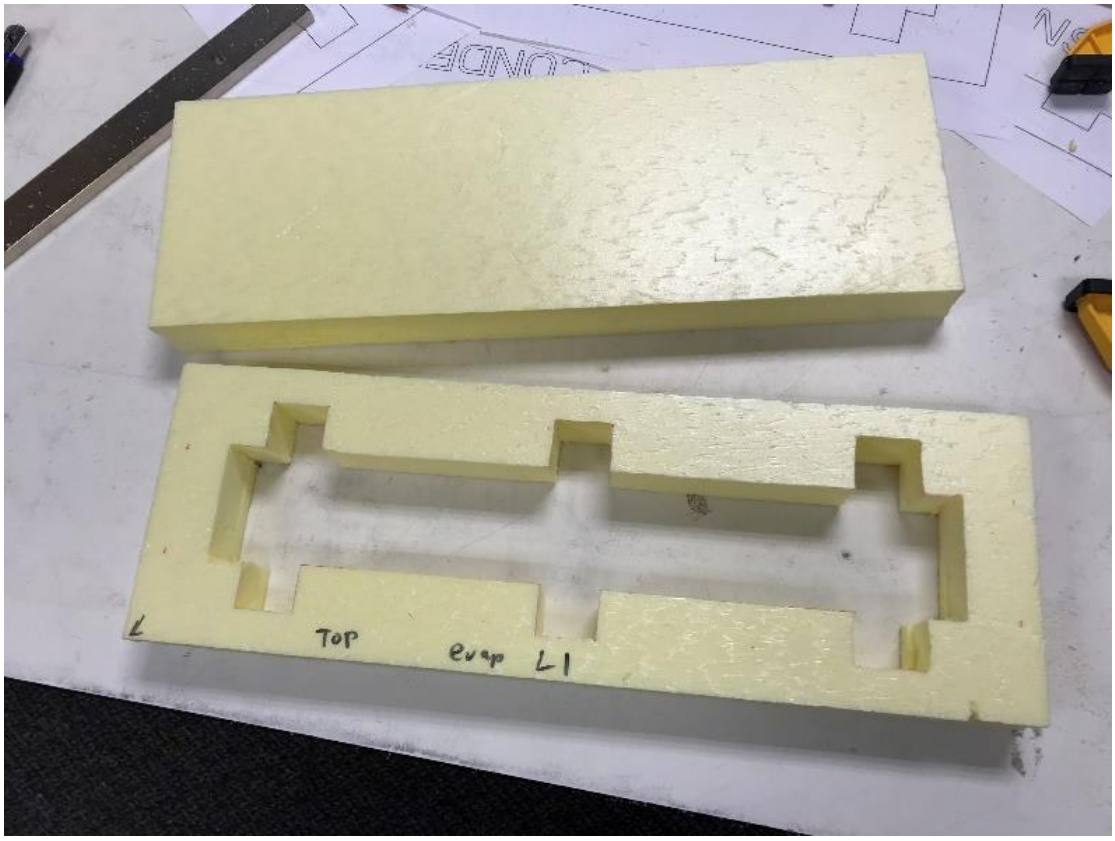

Figure 22. Evaporator insulation L1 layer.

Multiple layers of insulation foam sheets were joined together with adhesive to form the insulation systems for the evaporator section, condenser section, and the adiabatic

section. Figure 23 and Figure 24 show the exploded view and a fully assembled configuration of the insulation system assembly.

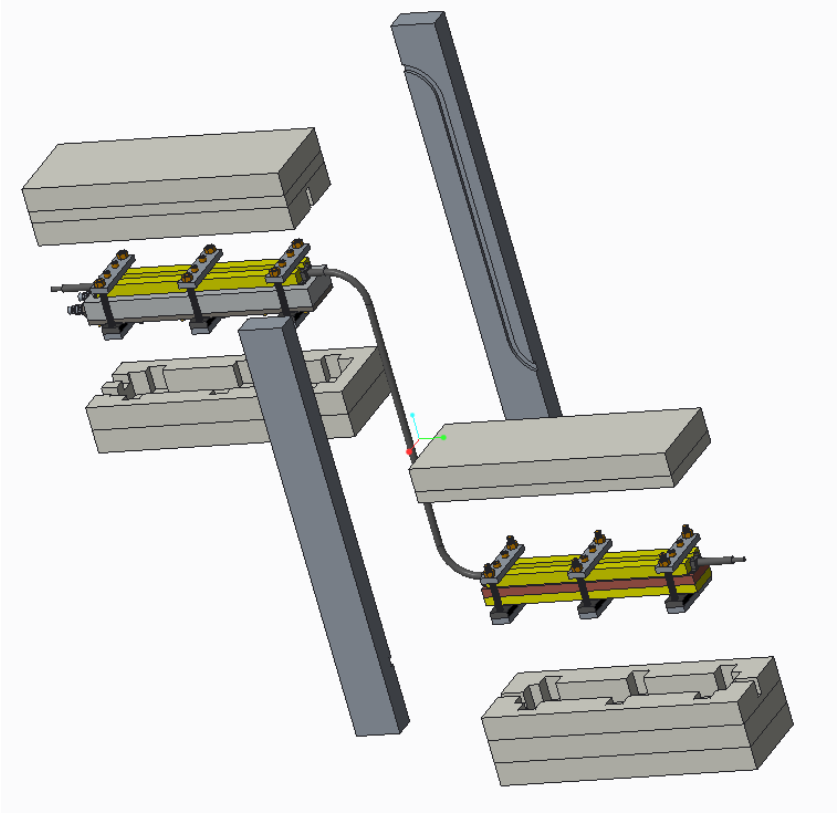

Figure 23. Insulation system exploded view.

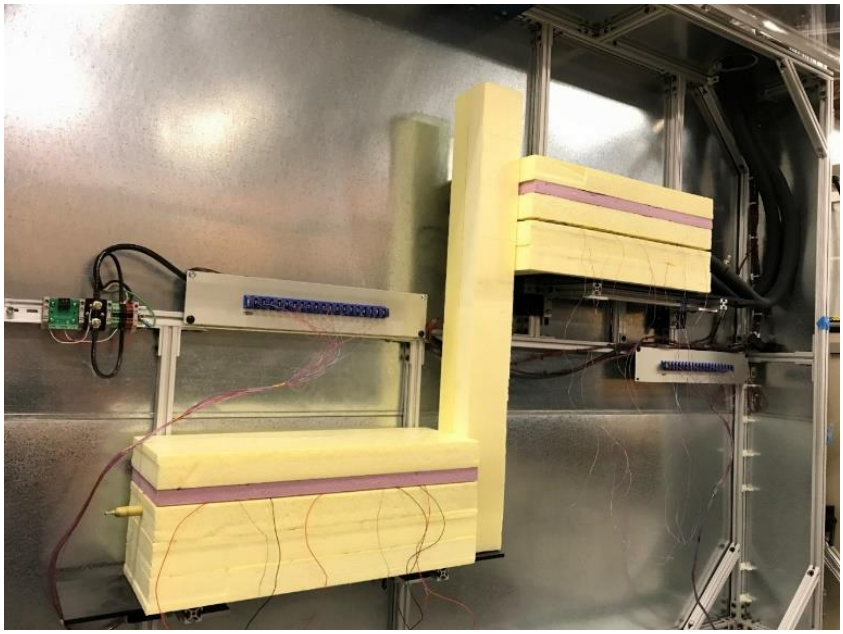

Figure 24. Insulated heat pipe assembly.

2.3.2 CFD Heat Loss Analysis

A CFD heat loss model was constructed in Comsol Multiphysics to understand the amount of heat loss present in the experiment. A range of constant temperature from -10 °C to 60 °C was applied to the internal walls of the evaporator and adiabatic section of the insulation system in the CFD model. Heat loss from the chiller block section of the heat pipe assembly was not needed to be accounted for as it is located downstream of the condenser flange on the conduction path as shown in the resistance network in Figure 25. No boundary condition settings were applied on the internal walls of the condenser section. Volumetric flow rate of 40 CFM was applied to the inlet of the controlled volume with air at 20°C. Volumetric flow rate setting of 40 CFM represents the inline fan operating without any back pressure. The inline fan operates at a lower volumetric

flow rate with the actual internal airflow impedance of the sheet metal enclosure which may lead to a slight overestimation of heat loss.

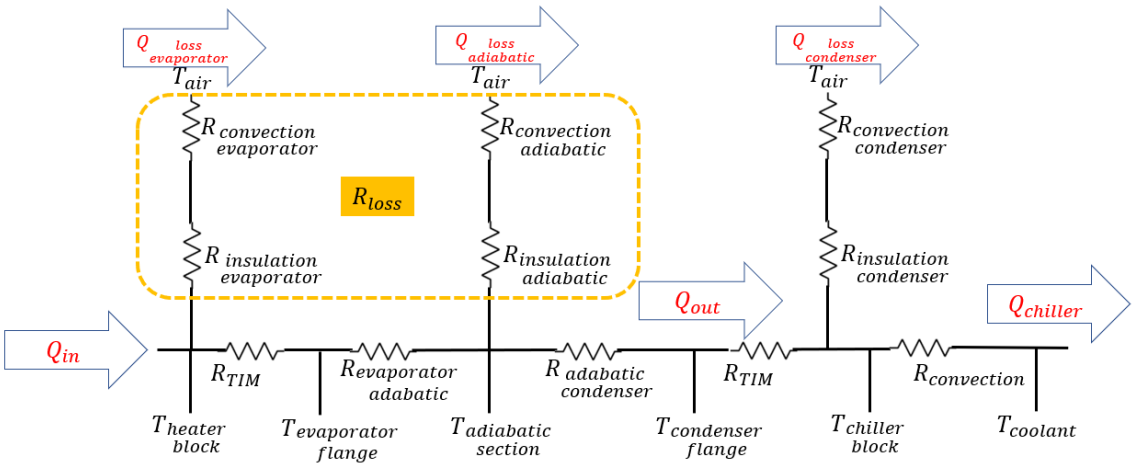

Figure 25. Thermal resistance network.

Figure 26 shows the internal surfaces where the temperature boundary condition is applied. Figure 27 shows the mesh element distribution used for the analysis. Figure 28 and Figure 29 show the temperature and air velocity pattern of the results.

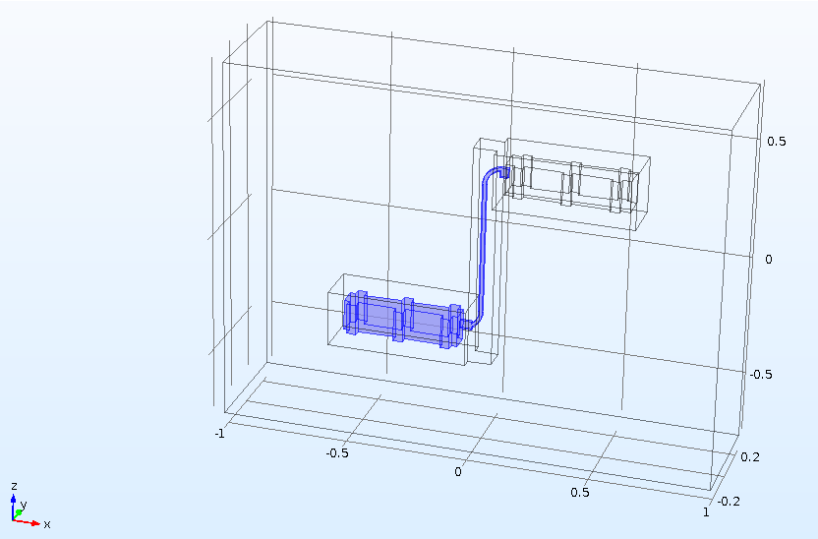

Figure 26. Temperature boundary condition surfaces.

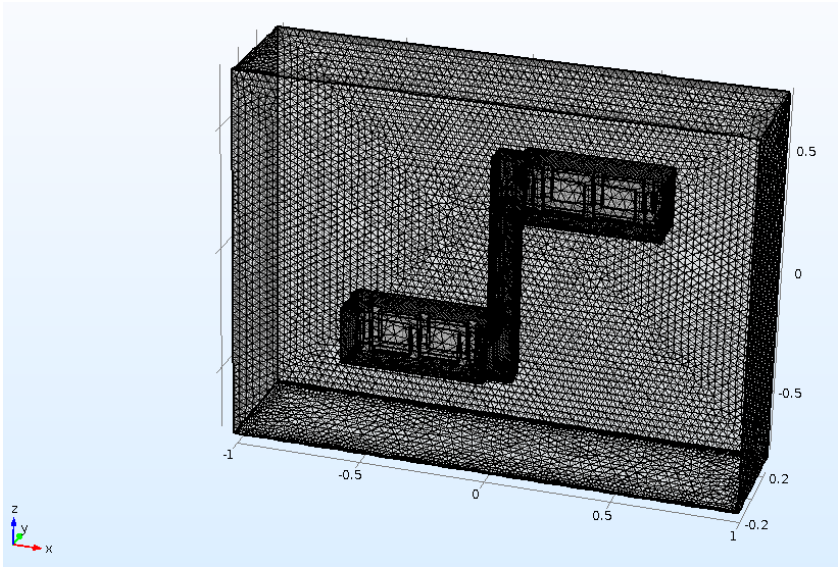

Figure 27. Mesh element distribution.

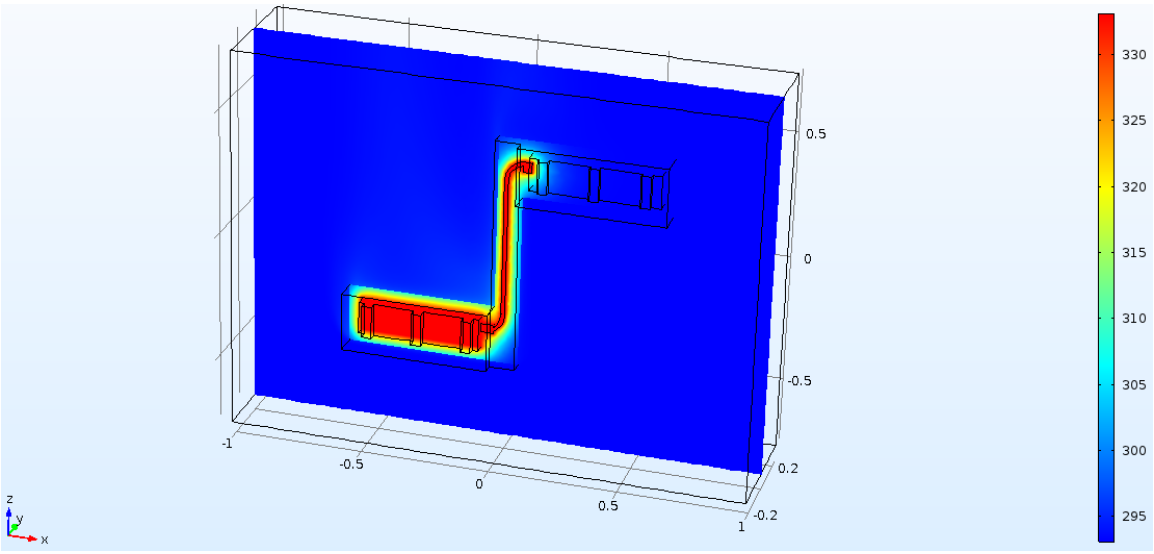

Figure 28. Temperature plot in kelvin.

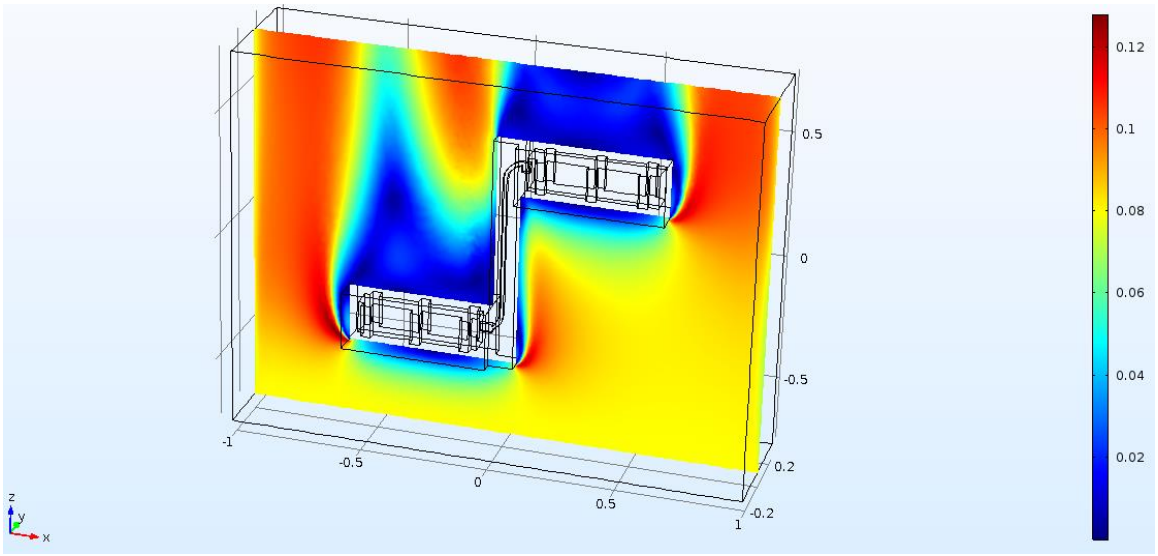

Figure 29. Air velocity plot in m/s.

The total amount of heat loss increases as temperature of the heat pipe elevates from room temperature. CFD results show the maximum amount of heat loss of 10W at 60ºC and no heat loss at 20ºC, about 3% of total heat input of 300W at 60ºC.

Table **3** and Figure 30 show the CFD heat loss analysis results. Equation 8 explains how a simplified thermal resistance, R_{loss}, is calculated by using evaporator temperature, adiabatic section temperature, ambient temperature, and the sum of heat loss from the evaporator and adiabatic section of the heat pipe, assuming the temperature difference between evaporator and adiabatic section is small.

$$R_{loss} = \frac{\frac{T_{evaporator} + T_{adiabatic}}{2} - T_{ambient}}{\dot{Q}_{\substack{loss \\ evaporator}} + \dot{Q}_{\substack{loss \\ adiabatic}}} \tag{8}$$

Table 3. CFD Heat Loss Analysis Results

Temperature [°C]	Heat Loss [W]	R_{loss} [°C/W]
60	10.2	3.92
50	7.7	3.90
40	5.1	3.92
30	2.6	3.85
20	0	N/A
10	-2.6	3.85
0	-5.2	3.85
-10	-7.7	3.90

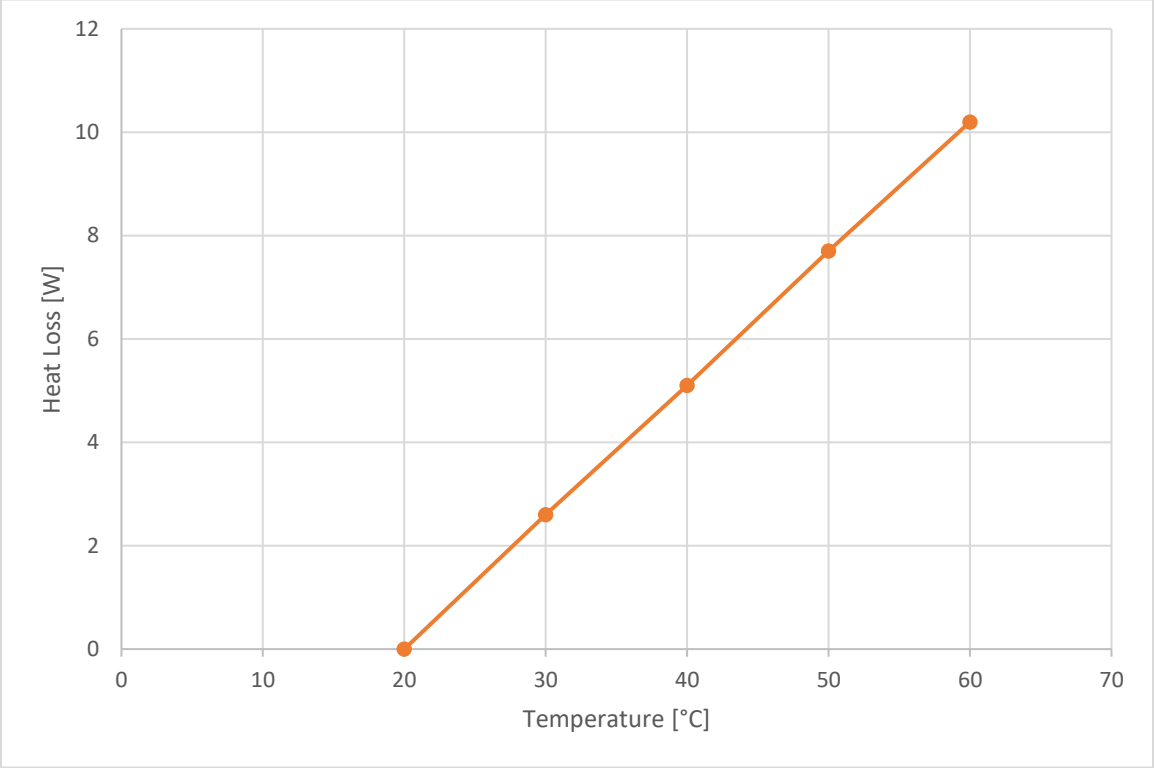

Figure 30. CFD heat loss vs. temperature analysis results.

The total power delivered from evaporator to condenser can be defined by subtracting heat loss from power input as described in Equation 9 and Equation 10.

$$\dot{Q}_{input} = P_{input} - \dot{Q}_{\substack{loss \\ evaporator}} - \dot{Q}_{\substack{loss \\ adiabatic}} \tag{9}$$

$$\dot{Q}_{input} = P_{input} - R_{loss}\left[\frac{T_{evaporator} + T_{adibatic}}{2} - T_{ambient}\right] \tag{10}$$

2.4 Physical Heat Loss Measurement

Physical heat loss measurements were conducted by elevating the evaporator and adiabatic section of the heat pipe assembly to match the temperature of the condenser to reach thermal equilibrium. The electrical power required for the heat pipe assembly to reach thermal equilibrium represents the total heat loss at the evaporator and adiabatic section. It is important to increase the electrical input power slowly over time to avoid any initiation of the boiling process inside the evaporator while elevating the temperature of the overall heat pipe assembly. A noticeable sudden temperature drop on the evaporator can be observed once the saturated liquid inside the evaporator begins to boil which is an indication of more than enough power is being applied to the heater block. Physical heat loss measurements were conducted from 30ºC to 60ºC in increments of 10ºC. Table 4 summarizes the amount of heat loss measured physically while Figure 31 compares the CFD heat loss results with the actual measurements. The results from

physical heat loss measurements align with the CFD heat loss analysis conducted in section 2.3.

Table 4. Physical Heat Loss Measurements

Heat Pipe Temperature [°C]	Ambient Temperature [°C]	ΔT [°C]	Heat Loss [W]	R_{loss} [°C/W]
59.9	17.2	42.7	11.5	3.71
50.1	18.4	31.7	9.0	3.52
40.3	17.7	22.6	5.5	4.11
30.4	18.0	12.3	3.0	4.13

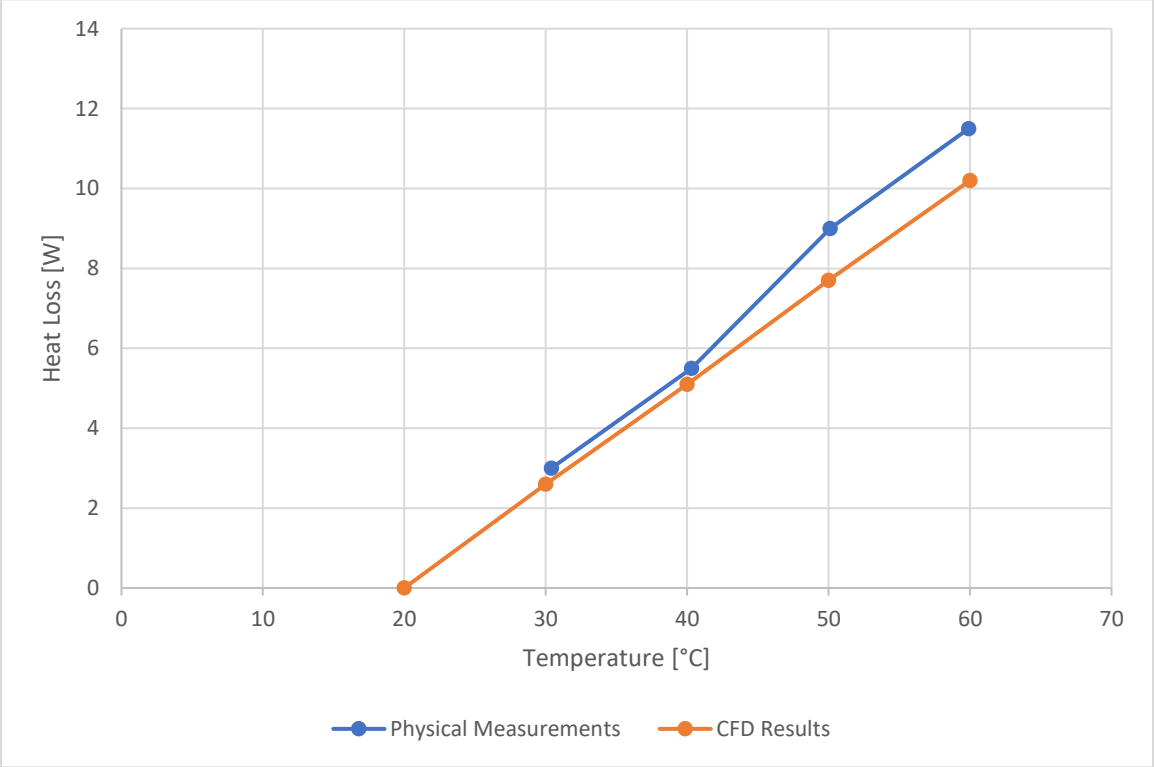

Figure 31. Physical vs. CFD heat loss comparison.

2.5 Nucleate Boiling Analysis

In order to initiate boiling of working fluid inside the evaporator, the internal heated surface temperature must be elevated above the saturation temperature of the working fluid. The rate of heat transfer of nucleate boiling is described in Equation 11 and the components used in the equation is explained in Table 5.

$$\dot{q}_{nucleate} = \mu_l h_{fg} \left[\frac{g(\rho_l - \rho_v)}{\sigma}\right]^{0.5} \left[\frac{C_{pl}(T_s - T_{sat})}{C_{sf} h_{fg} {Pr_l}^n}\right]^3 \quad (11)$$

Table 5. Nucleate Boiling Equation Components

Terms	Description	Units
$\dot{q}_{nucleate}$	Nucleate Boiling Heat Flux	W/m²
μ_l	Viscosity of the Liquid	kg/m·s
h_{fg}	Enthalpy of Vaporization	J/kg
g	Gravitational Acceleration	m/s²
ρ_l	Density of the Liquid	kg/m³
ρ_v	Density of the Vapor	kg/m³
σ	Surface Tension of Liquid-Vapor Interface	N/m
C_{pl}	Specific Heat of the Liquid	J/kg·°C
T_{excess}	Excess Temperature, $T_s - T_{sat}$	°C
T_s	Temperature of the Heated Surface	°C
T_{sat}	Saturation Temperature of the Fluid	°C
C_{sf}	Experimental Surface-Fluid Constant	
Pr_l	Prandtl Number of the Liquid	
n	Experimental Fluid Constant	

Fluid properties used in Equation 11 are functions of temperature and pressure. Temperature of the heated surface is a component of interest that was closely examined along with the start-up power requirement. Viscosity and surface tension of the working fluid are two major components which affects the heated surface excess temperature, $T_s - T_{sat}$. They both decrease as the saturation temperature increases. Figure 32 and Figure 33 show the relationship between liquid viscosity and surface tension of the working fluid over its operating temperature.

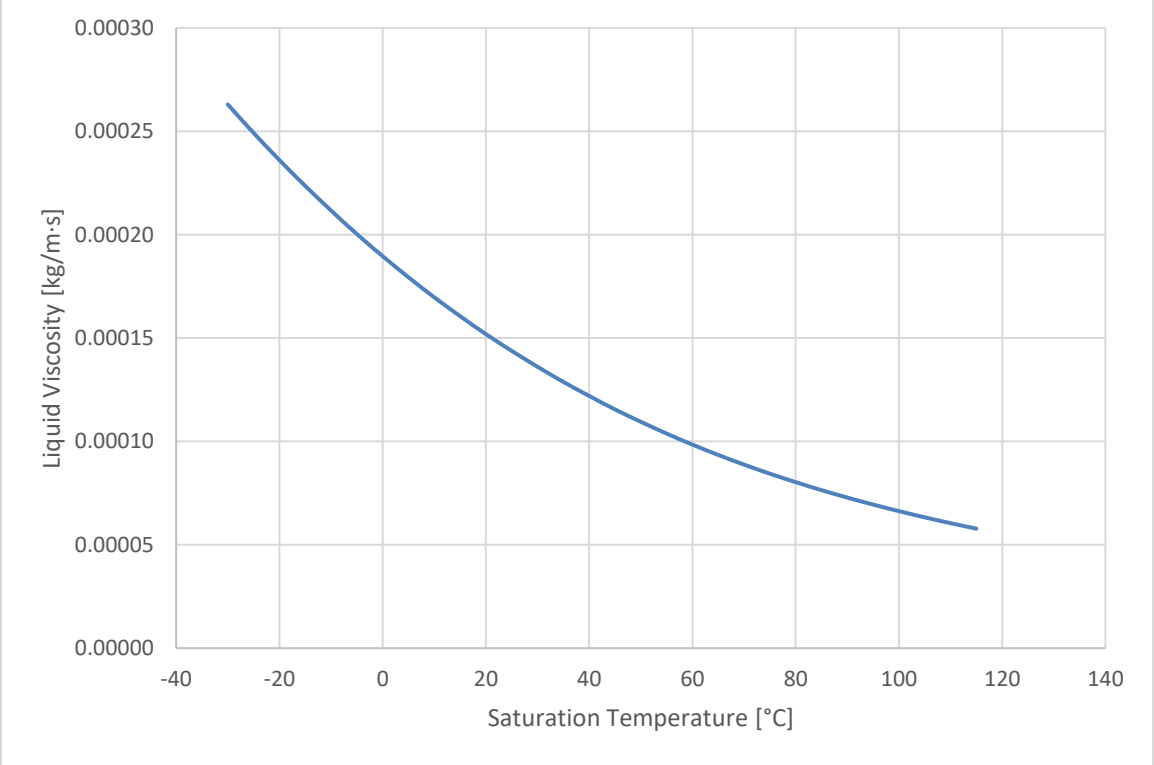

Figure 32. Ammonia NH3 liquid viscosity vs. saturation temperature [8].

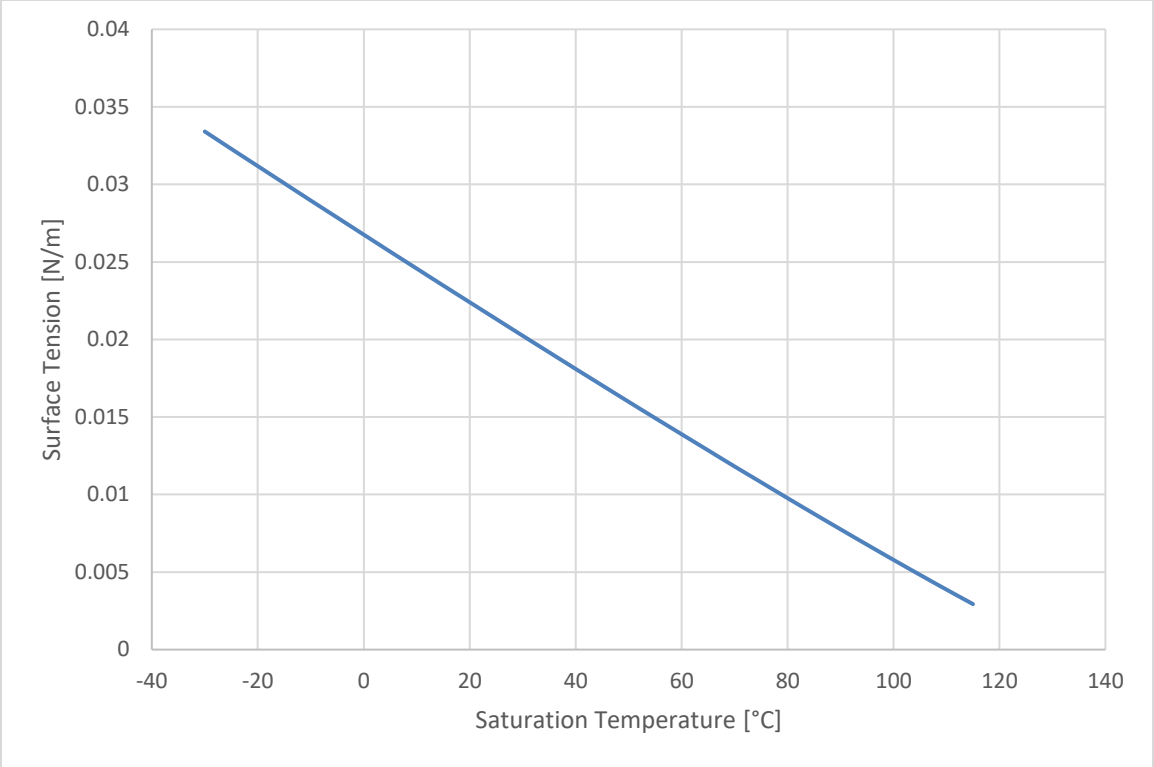

Figure 33. Ammonia NH3 surface tension vs. saturation temperature [8].

The heated surface excess temperature increases marginally to offset for the difference caused by decrease in viscosity and surface tension to maintain a constant nucleate boiling heat flux in Equation 9 when the saturation temperature of the fluid increases. The heated surface temperature for a range of saturation temperatures from 20°C to 60°C in increments of 10°C were calculated by setting the nucleate boiling heat flux to a constant. Figure 34 shows the correlation of heated surface temperatures vs. fluid saturation temperatures.

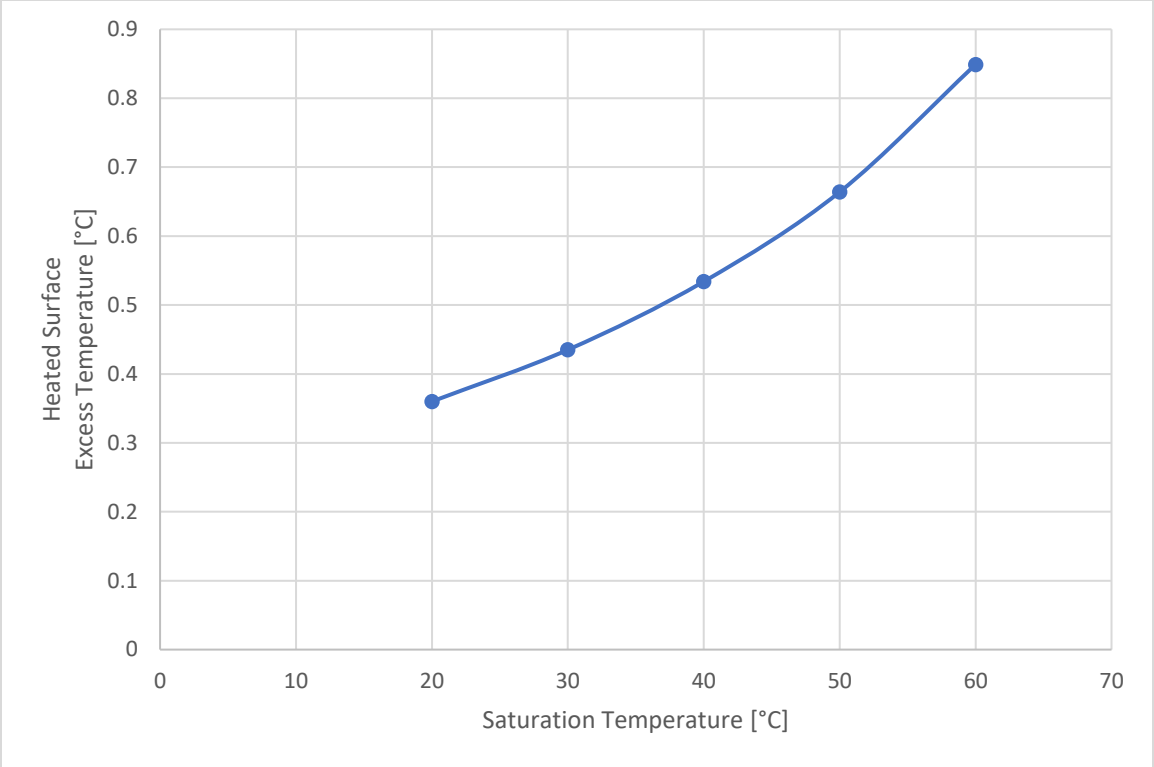

Figure 34. Heated surface excess temperature vs. saturation temperature.

3.0 Experimental Work

3.1 Heater Block Assembly

The heater block provides and spreads the heating load applied to the heat pipe evaporator. It acts as a thermal mass to dampen any sudden changes in heat transfer rate to maintain an isothermal heat transfer surface for the heat pipe evaporator. The heater block is placed between the evaporator flange and the heating element. An array of resistance heating elements was selected to be able to provide 300W of heating load for the heater block. Figure 35 shows a single resistance heating element.

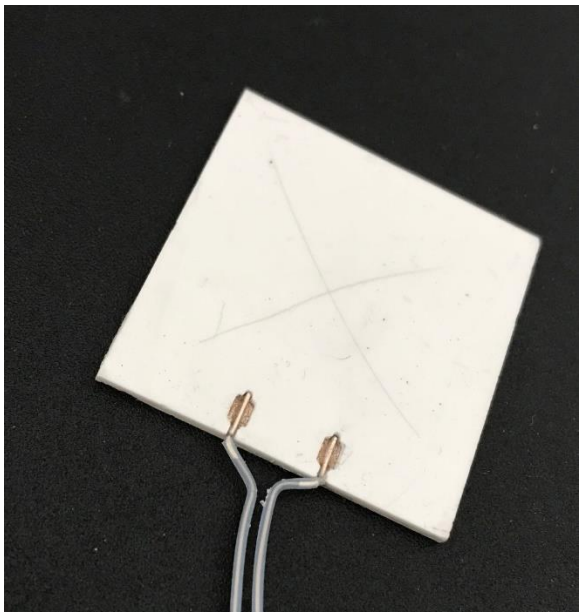

Figure 35. Resistance heating element 40mm x 40mm x 2mm .

The heater block consisted of a fiberglass backing plate, a 0.75” thick copper plate, resistance heating elements, thermal interface material, and mechanical fasteners to assemble the heater block together. Figure 36 shows the exploded view of the overall heater block design.

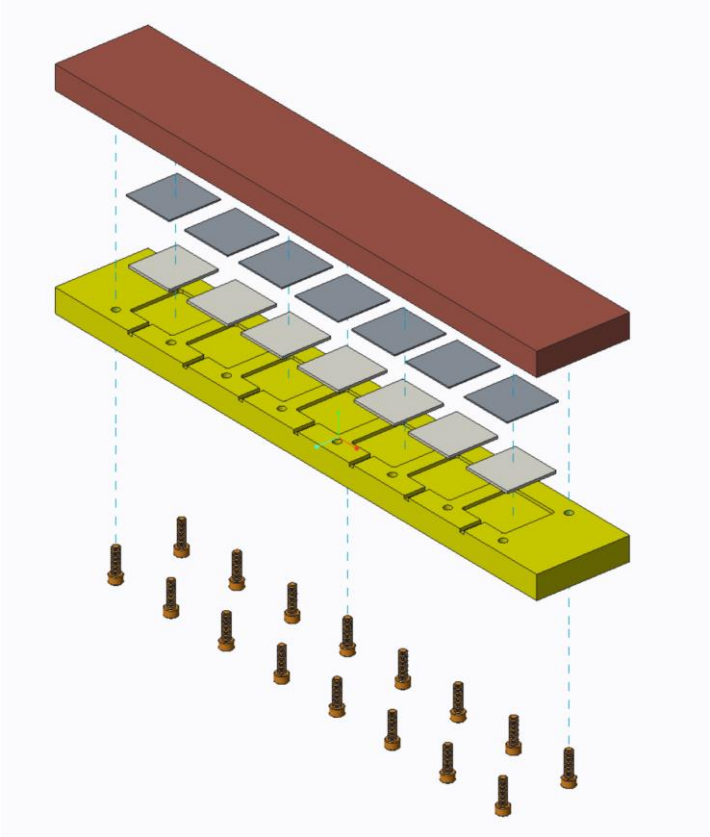

Figure 36. Heater block exploded view.

Silicone thermal interface material was used to conduct heat from the resistance heating elements to the copper plate. Thermocouples were installed between the thermal interface material and copper plate. Mechanical features were designed into the fiberglass backing plate to precisely control the positions of resistance heating elements and thermal interface material compression. Figure 37 and Figure 38 show the resistance heating element placement with thermocouple and thermal interface material installed on the fiberglass backing plate.

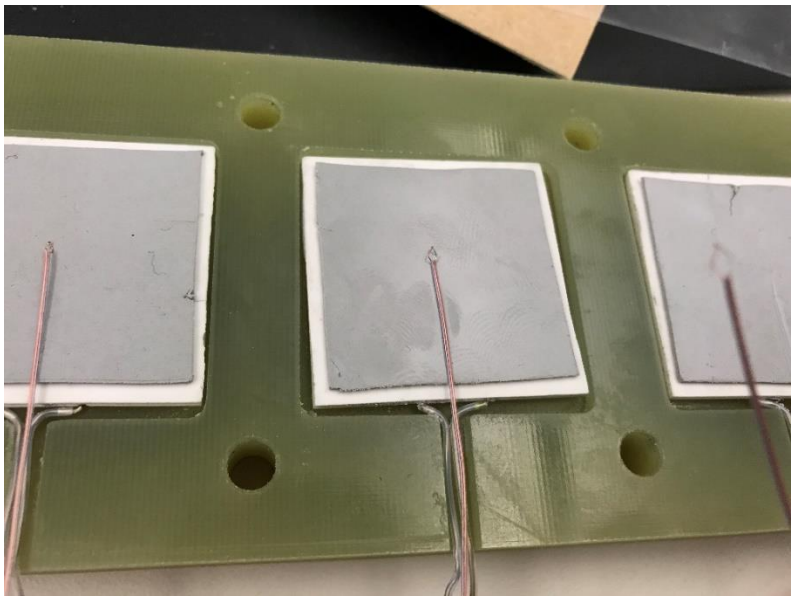

Figure 37. Resistance heater and TIM configuration.

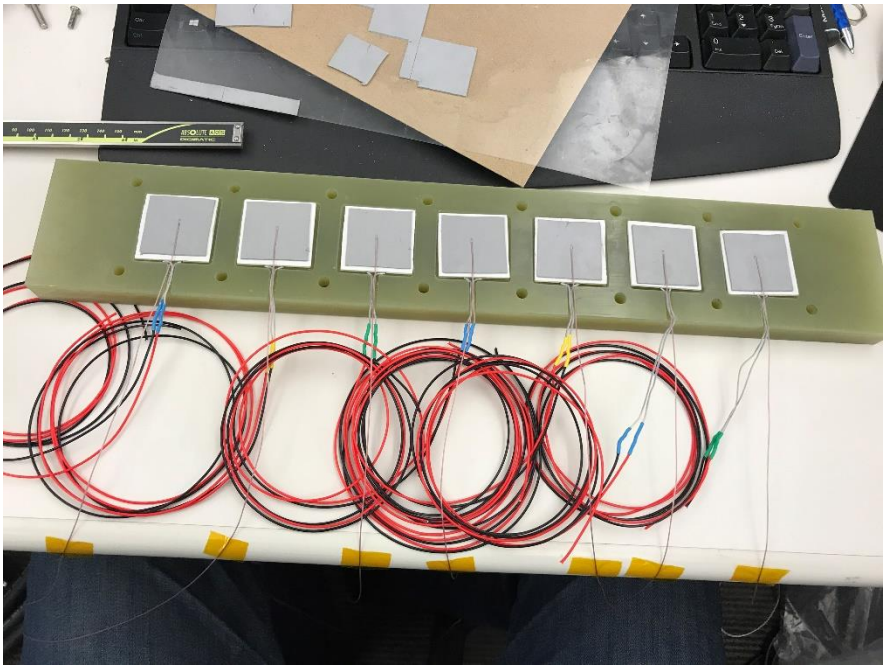

Figure 38. Resistance heater array installed on backing plate.

Stainless steel fasteners were used to evenly compress the thermal interface material across all the resistance heating elements. Figure 39 to Figure 41 show the assembled heater block, heater block assembled onto the evaporator assembly, and cross-sectional view of the evaporator assembly.

Figure 39. Assembled heater block.

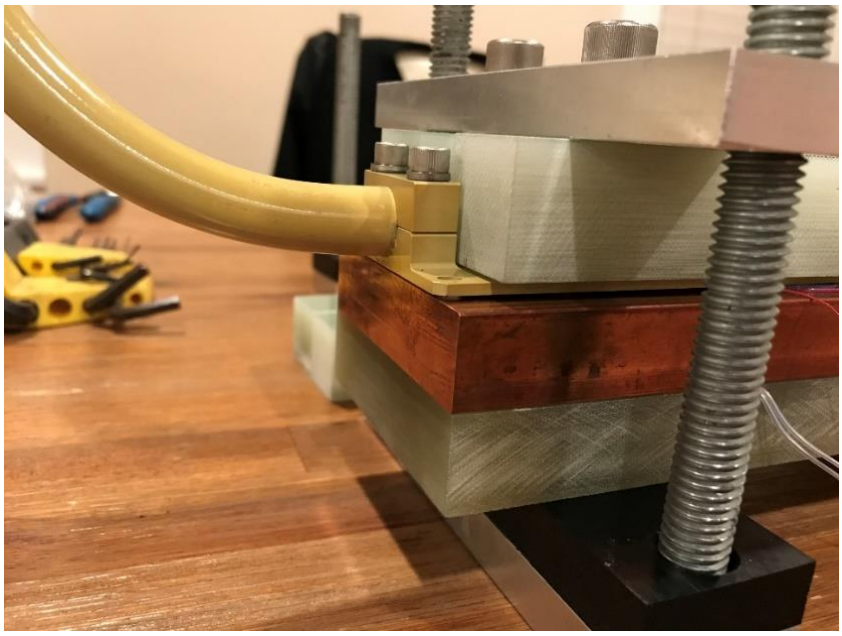

Figure 40. Heat pipe evaporator assembly.

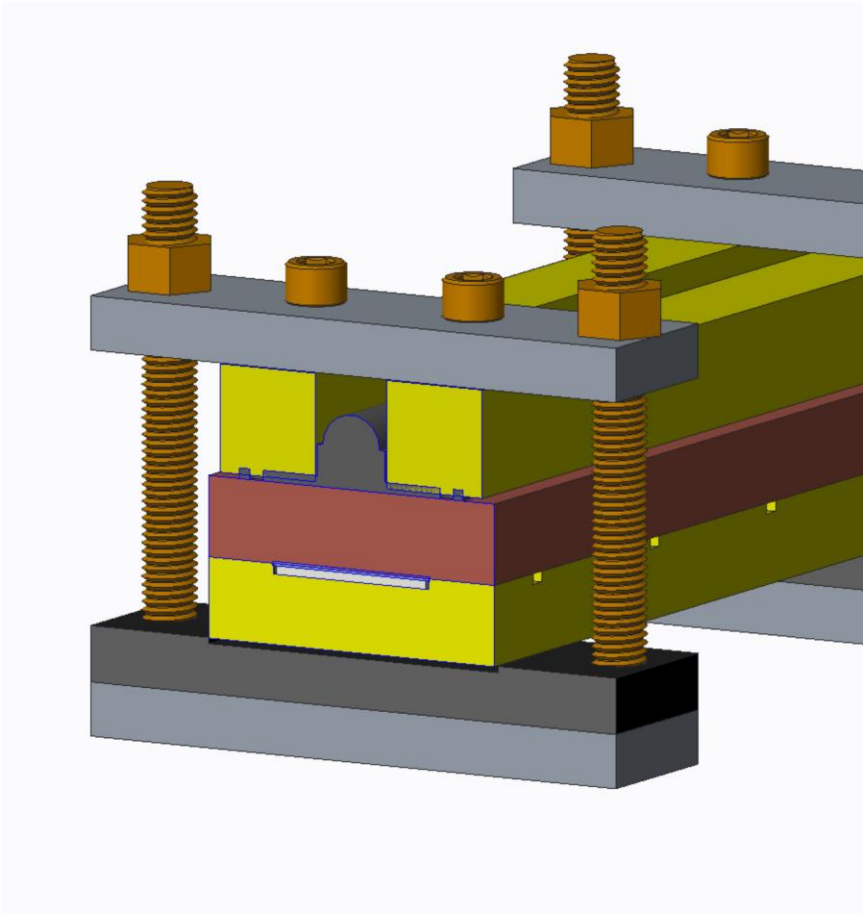

Figure 41. Evaporator assembly cross-sectional view.

3.2 Chiller Block

A chilled water cold plate was used to extract heat from the condenser. The cold plate was constructed entirely from T6-6061 aluminum. Temperature-controlled coolant was supplied to the cold plate at a volumetric flowrate of 5 GPM to provide an isothermal heat

transfer surface for the condenser flange. Figure 42 shows the cold plate assembly and Figure 43 shows the cross-sectional view of the cold plate assembly.

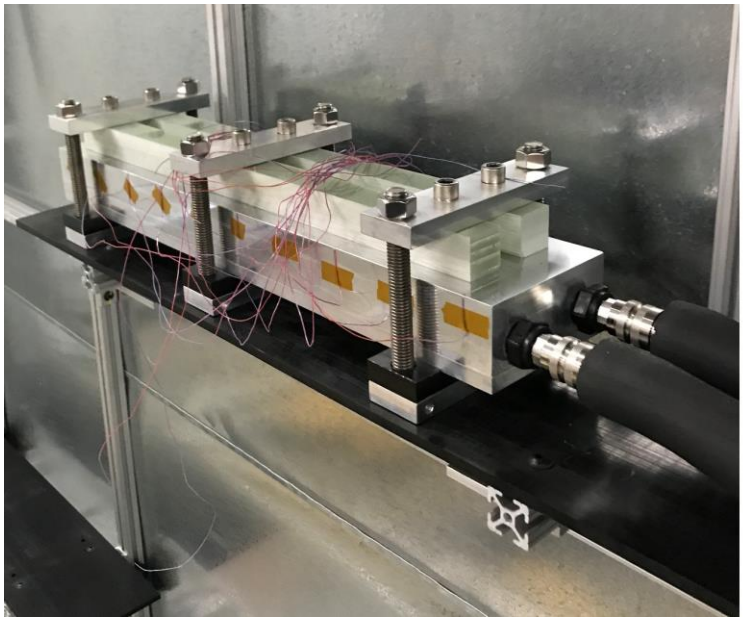

Figure 42. Chiller block assembly.

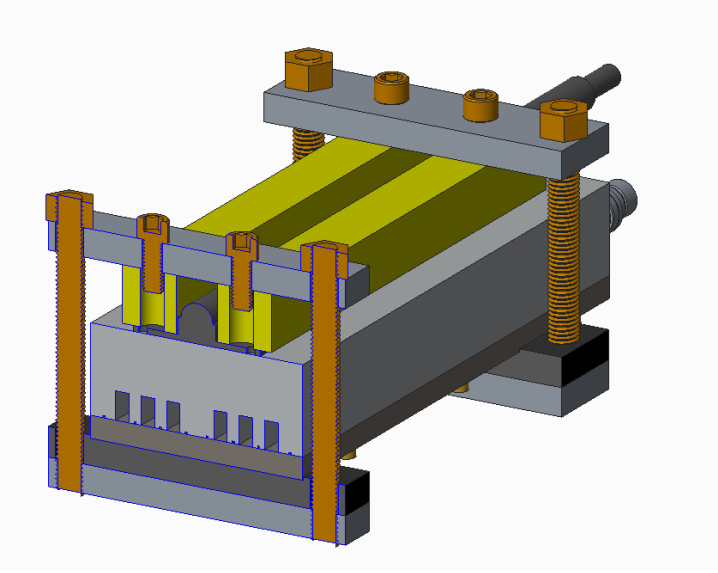

Figure 43. Chiller block cross-sectional view.

3.3 Mechanical Retention System

A mechanical retention system was designed to provide adequate compression force across the thermal interface material between the evaporator and condenser. The mechanical retention system consisted of aluminum plates, fiberglass plates, and mechanical fasteners. The aluminum plates provided mechanical structure to provide compression force. The fiberglass plates provided thermal insulation against the evaporator and condenser surfaces. Stainless steel mechanical hardware provided compression force against thermal interface material upon tightening. The identical mechanical retention system was used on the evaporator and condenser assembly of the thermosyphon. Figure 44 shows the exploded view of the mechanical retention system. Figure 45 shows the mechanical retention system installed onto the condenser of the heat pipe assembly.

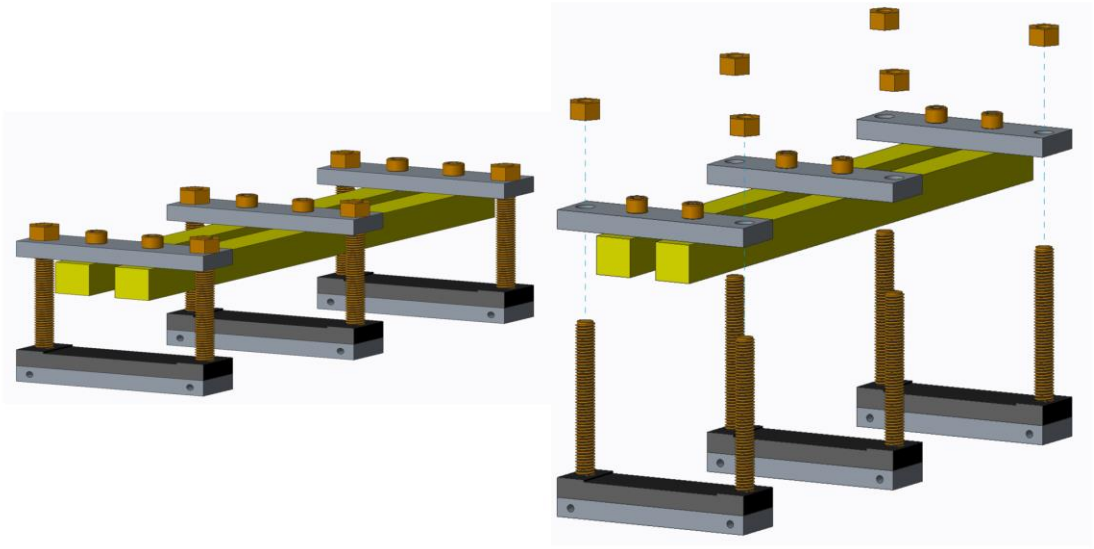

Figure 44. Evaporator and condenser mechanical retention system.

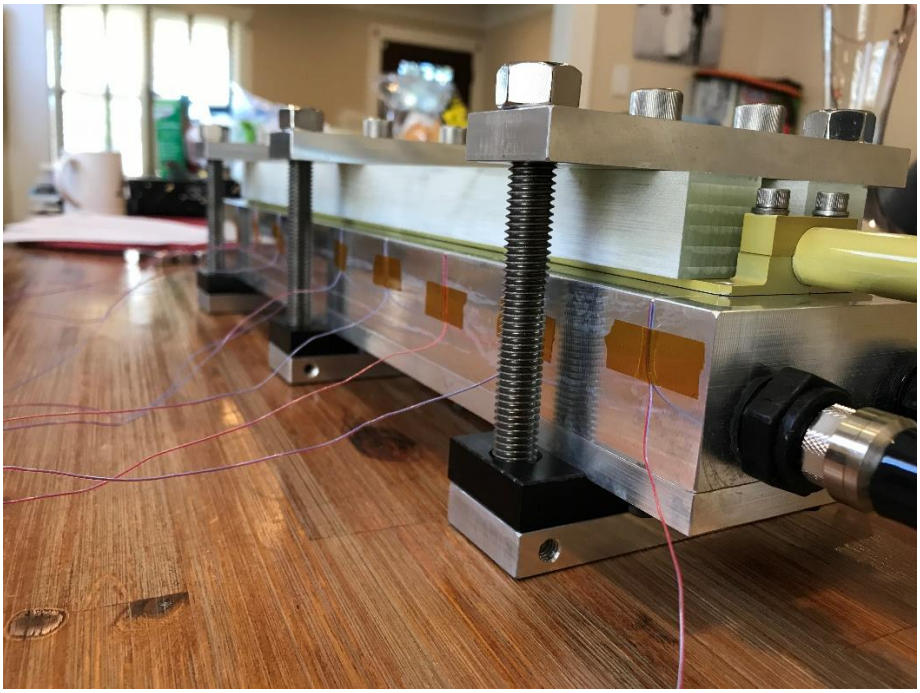

Figure 45. Mechanical retention system installed on condenser.

3.4 Thermal Interface Material

A silicone compound gap filler type thermal interface material was selected for its compressibility and thermal conductivity. It is important for thermal interface material to fill the gap between the heat pipe flanges, heater, and chiller blocks over a large surface area. The thermal interface material has a silicone compound composition with a thermal conductivity of 6 W/mk and an initial thickness of 1 mm. It was expected to achieve 50% compression to reach a final thickness of 0.5 mm upon mechanical compression. A physical compressions test showed that the selected thermal interface material was able to evenly fill up the gap between the evaporator flanges and the heater and chiller blocks.

Figure 46 and Figure 47 show that the thermal interface material was evenly compressed by the mechanical retention system over the large heat transfer surface area.

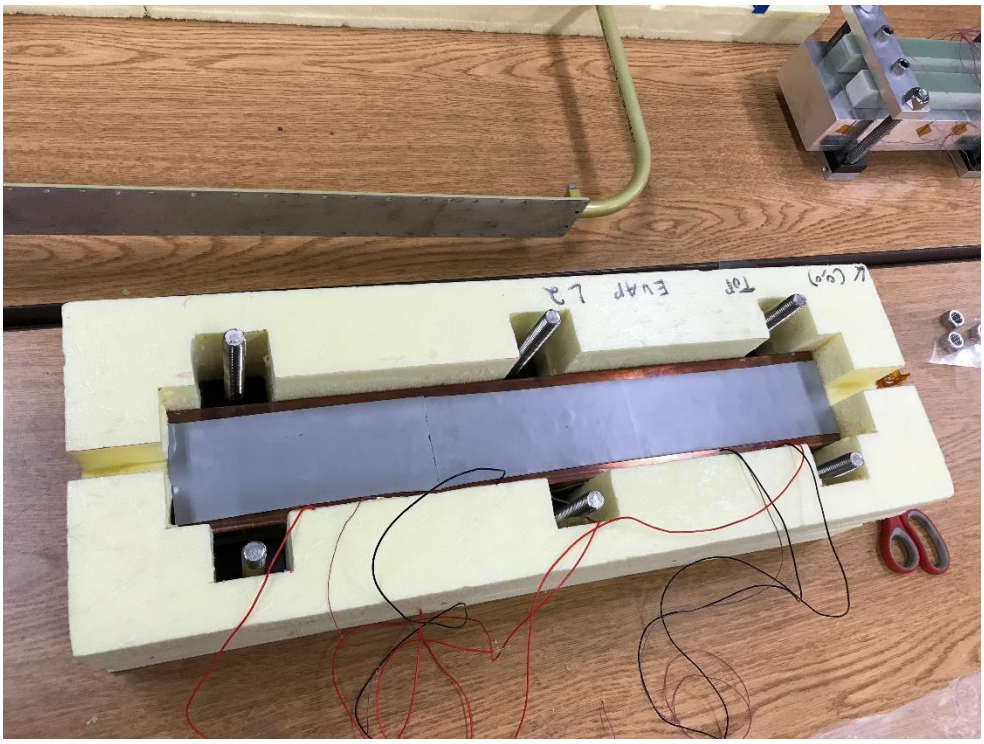

Figure 46. Thermal interface material before compression.

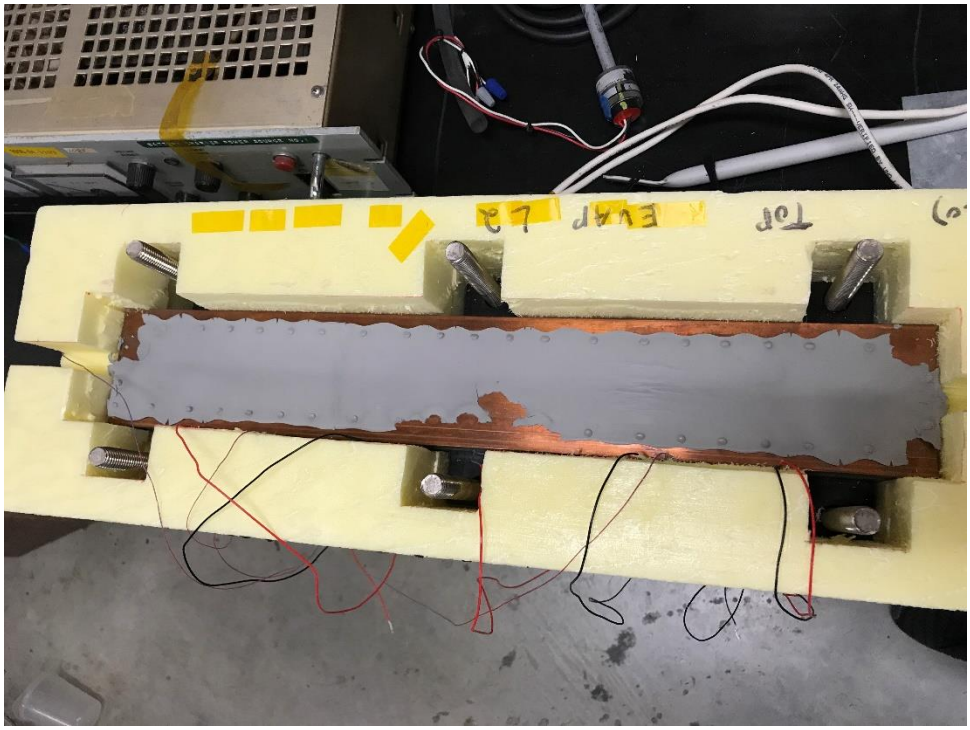

Figure 47. Evenly compressed thermal interface material.

3.5 DC Power Supply

The electrical power consumption of the electrical resistance heating element was measured for heat input calculation. Electrical energy is transformed into thermal energy at the resistive coils inside the resistance heating elements. Each individual heating resistance element has an electrical impedance of 6Ω at 20°C, and they were configured in parallel. Figure 48 shows the electrical configuration of the resistance heating elements.

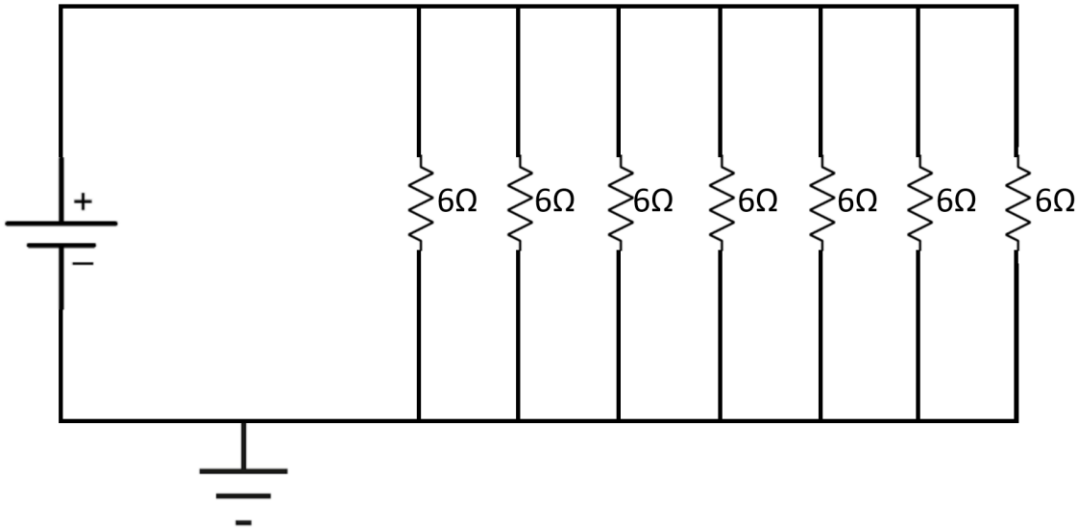

Figure 48. Heater block electrical impedance diagram.

DC power was selected to power the resistance heating elements. The DC power supply needed to deliver 20VDC of voltage and 14A of current to provide 300W of heat to the evaporator. A Chroma 62024P-80-60 DC programmable power supply was selected for its ability to deliver the required voltage and current. The selected power supply is also programmable. A series of power output can be preprogrammed into the power supply for test automation capabilities. Figure 49 and Figure 50 show the programmable DC power supply and the Chroma software interface.

Figure 49. Programmable DC power supply.

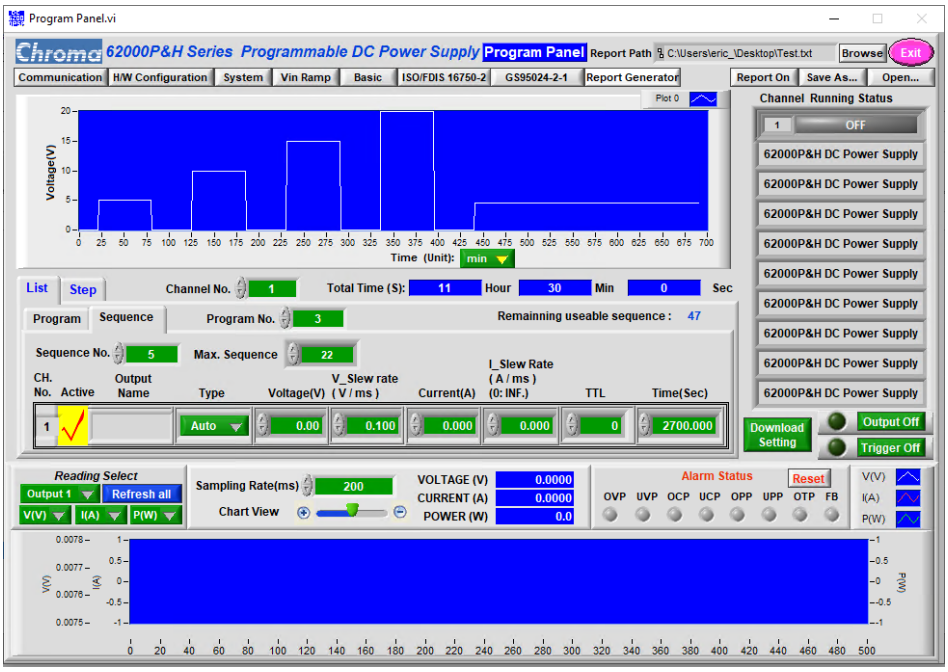

Figure 50. Chroma soft panel interface.

The DC voltage and current were distributed across each individual resistance heating element using din rail terminal blocks. Electrical current supplied to the resistance heating elements was measured with a shunt resistor wired in series with the DC power

supply. Voltage was measured at the din rail terminal blocks. Figure 51 shows the DIN rail electrical distribution unit.

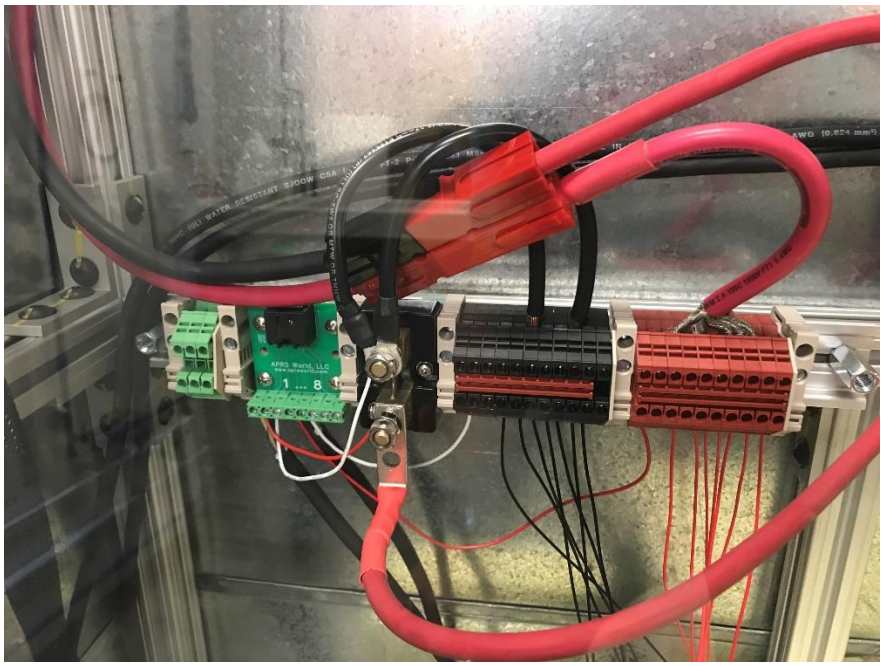

Figure 51. DC electrical distribution terminal blocks.

3.6 Water Chiller

The water chiller malfunctioned and failed to maintain a constant chilled water bath temperature due to electronic component failures in the control circuit. The original control circuit was not able to maintain the chilled water bath temperature at set point. It caused the chilled water supply temperature to fluctuate beyond acceptable range for the heat pipe testing processes to reach steady state. The water chiller's temperature stability was restored by replacing the control circuit and some corresponding electromechanical components. Installing a new temperature controller was considered instead of repairing the original control circuit. The new temperature controller improved the water chiller's

capabilities by adding remote controlled capabilities onto the water chiller. Figure 52 shows the malfunctioned control circuit.

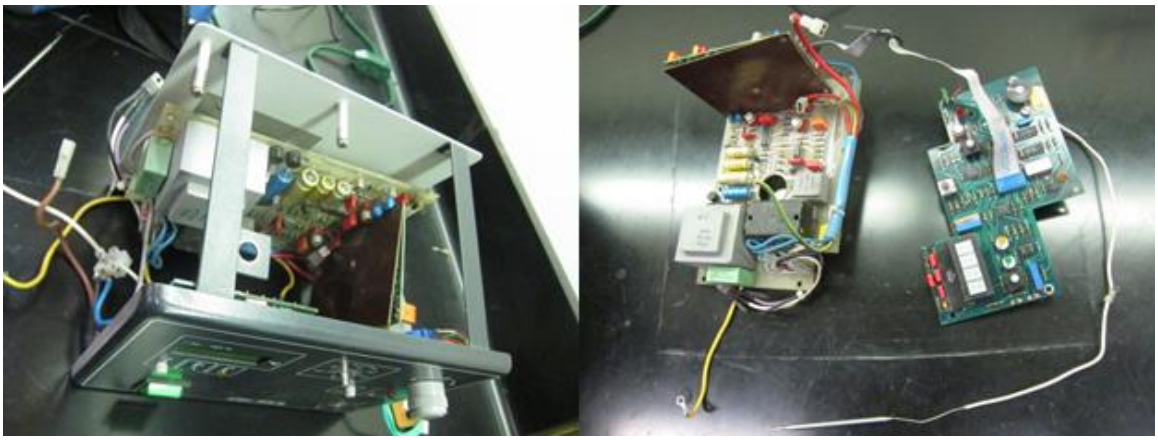

Figure 52. Malfunctioned control circuit.

A temperature controller with serial communication feature was selected. An Omega CNi32 series PID temperature controller was installed to control the chilled water temperature by throttling the refrigerant solenoids. The controller has the capability to be programmed remotely with RS-232 or RS-485 communication protocols. Figure 53 shows the Omega CNi32 PID temperature controller.

Figure 53. Omega CNi32 PID temperature controller.

All the original electronic components were removed from the water chiller before the redesigned control circuit and temperature controller were installed. The redesigned control circuit consists of a 24VDC power supply, two DC solid state relays, an Atmel Atmega 328P microcontroller, a 24VDC to 5VDC DC-DC switching regulator, and two 24VDC refrigerant solenoids. The temperature controller has a DPST, double pole single throw relay which can be used to energize the two refrigerant solenoids. Instead of energizing the refrigerant solenoids directly with the DPST relay on the temperature controller, two solid state relays and a programmed microcontroller are used to energize the refrigerant solenoids to reduce wear and tear on the temperature controller's DPST relay. The microcontroller senses high and low signals from the temperature controller and sends digital signals to the solid-state relays for refrigeration solenoids throttling. Figure 54 to Figure 56 show the new control circuit installed onto the water chiller.

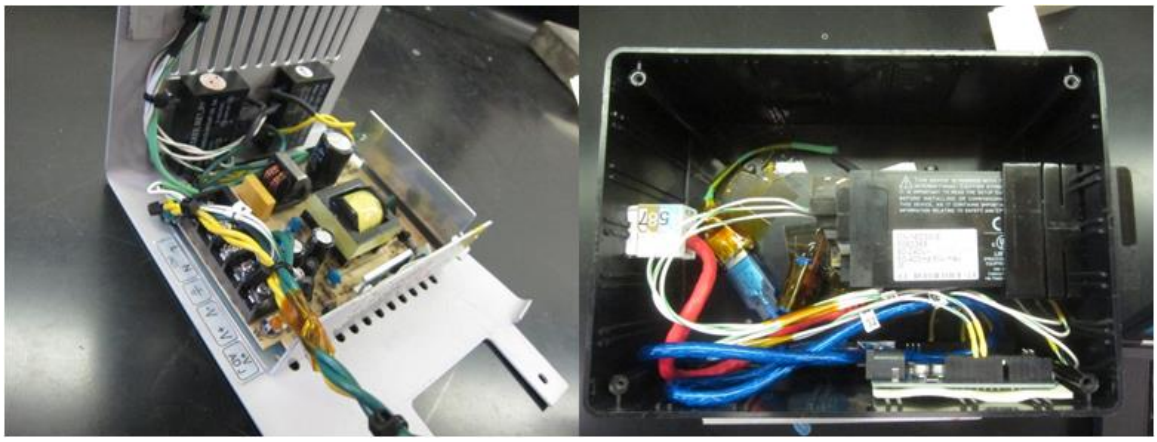

Figure 54. Water chiller control circuit components.

Figure 55. New water chiller control circuit.

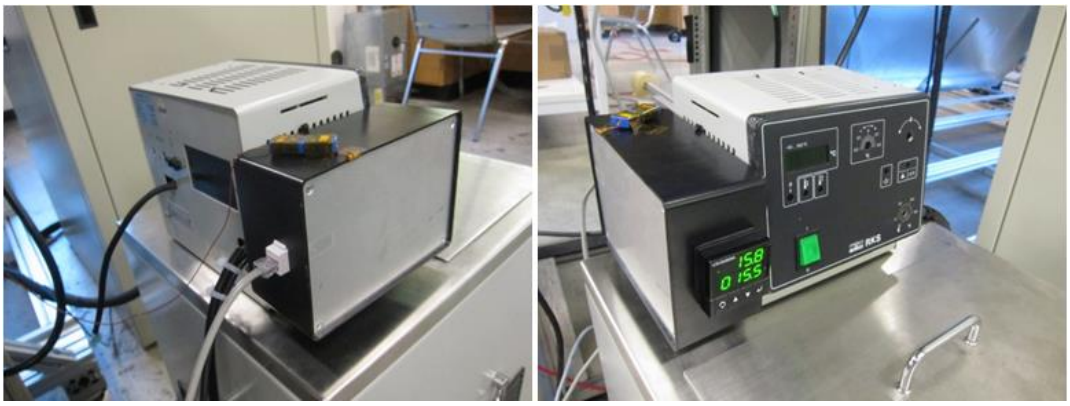

Figure 56. New water chiller circuit installed.

The temperature controller was programmed with a proportional gain value of 30, integral value of 0, derivative value of 0, and a cycle time of 3 seconds. It is able to maintain the chilled water bath within +/- 0.1 °C. Figure 57 shows the chilled water bath temperature response with a sudden drop of heat load from 275W to 50W over time.

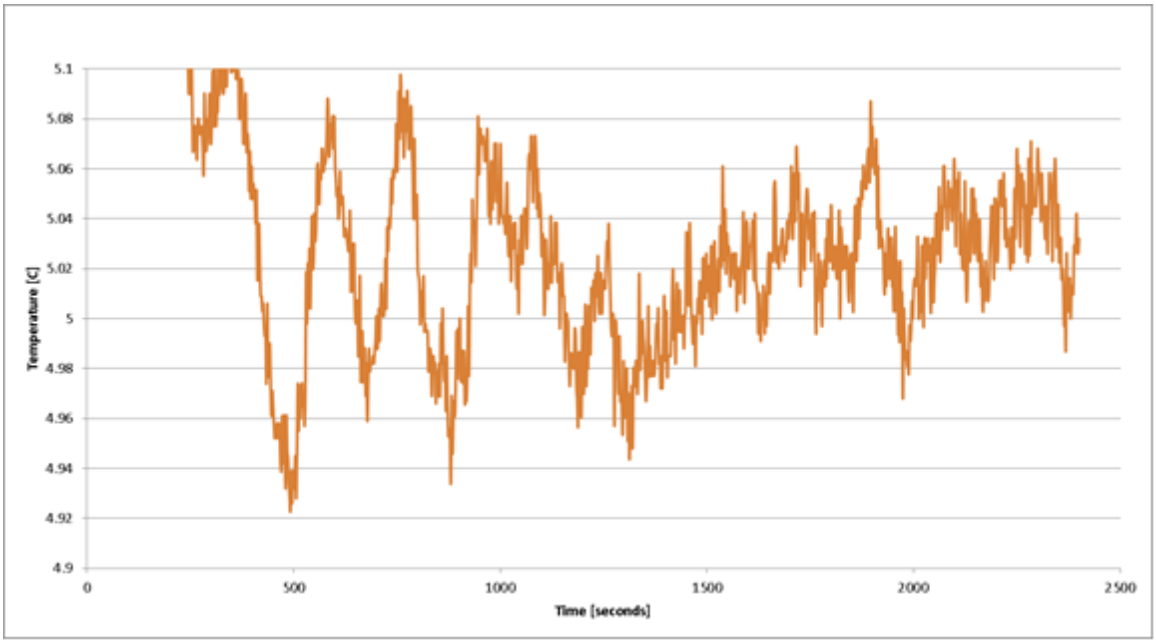

Figure 57. Chilled water bath temperature response graph.

3.7 Thermocouple Locations

Type T thermocouples were used in this experiment. Thermocouples were instrumented throughout the body of the heat pipe. A total of 12 thermocouples were used for acquiring temperature readings on the heat pipe body. Heat loss is modeled with four thermocouples. Figure 58 shows the actual positions of the thermocouples mounted on the heat pipe during testing.

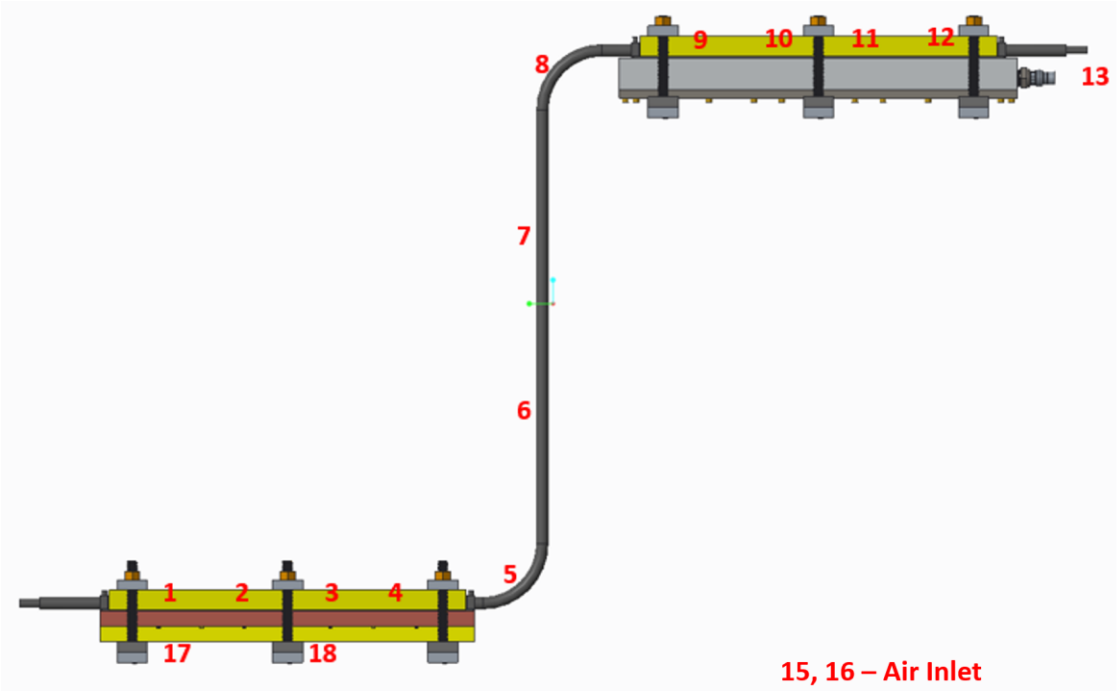

Figure 58. Locations of thermocoples on heat pipe assembly.

Channels 1 to 4 were mounted on the evaporator body to acquire evaporator readings. Channels 9 to 12 were mounted on the condenser body to acquire condenser readings. Figure 59 and Figure 60 show the location of thermocouples 1-4 and 9-12 on the evaporator and condenser body.

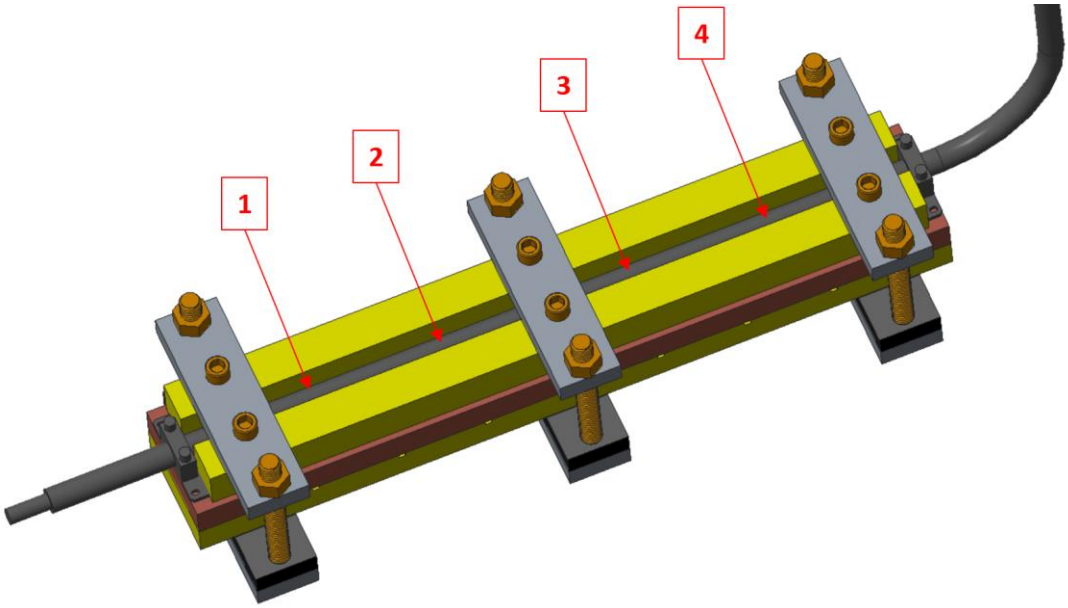

Figure 59. Locations of thermocoples on evaporator body.

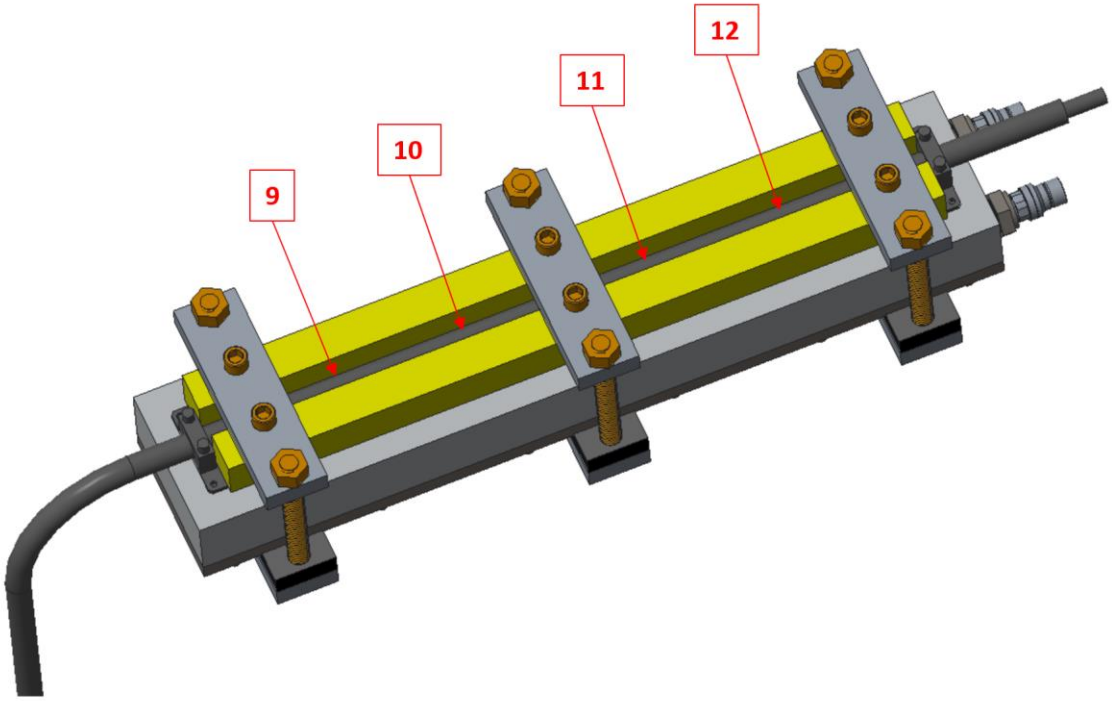

Figure 60. Locations of thermocoples on condenser body.

3.8 Uncertainty Analysis

The total temperature uncertainty on a single channel of thermocouple temperature measurement can be defined as described in Equation 12 and Equation 13.

$$U_{total} = \sqrt{{U_{bias}}^2 + {U_{random}}^2} \tag{12}$$

$$U_{bias} = \sqrt{(T_{thermocouple} - T_{thermometer})^2} \tag{13}$$

A hot plate with a magnetic stirrer was used to provide a constant temperature bath for determining the bias uncertainty and random uncertainty of the thermocouples. Random error of the new thermocouples was determined by taking 30 fast readings in an isothermal water bath. The standard deviation of the 30 readings was used to determine the random error. Figure 61 shows the temperature calibration setup.

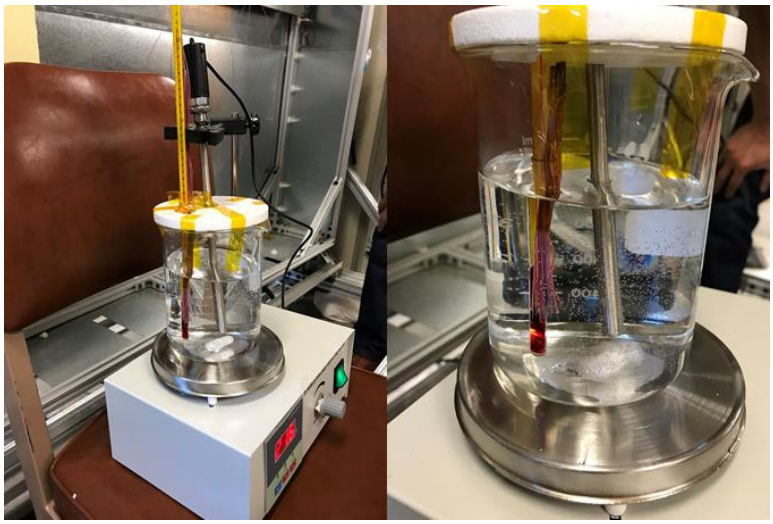

Figure 61. Thermocouple calibration setup.

The bias uncertainty was determined to be 0.31°C. The random error was analyzed to be 0.04°C. The total temperature uncertainty was calculated to be 0.31°C.

The Agilent data logger has a voltage measurement accuracy of 0.0026%. The total power input, P_{input} uncertainty was determined to be 0.0052 %. Physical heat loss uncertainty was calculated to be 1.2 W. Thermal conductivity uncertainty was calculated to be 0.44%. The total heat transfer from evaporator to condenser, $\dot{Q}_{input}$ uncertainty is 1.2 W. Table 6 summarizes the experimental uncertainty findings.

Table 6. Experimental Uncertainty Table

Measurement	Experimental Uncertainty
Temperature	0.31°C
P_{input}	0.01%
$\dot{Q}_{loss}$	1.2W
$\dot{Q}_{input}$	1.2W
k	0.44%

4.0 Results and Discussion

Start-up tests were performed on the S shaped thermosyphon heat pipe. The start-up tests were conducted from 20°C- 60°C in a 10°C initial starting temperature with tilt angles of 0-90° in increments of 10°. Temperature-controlled coolant was initially supplied to the condenser. Temperature readings of the heat pipe assembly were being constantly monitored during the test. A constant heat load was supplied to the evaporator once the whole heat pipe assembly reached the initial start-up temperature. Start-up was determined from a noticeable temperature decrease at the evaporator body which

indicates the initiation of nucleate boiling inside the evaporator. Figure 62 and Figure 63 show examples of the start-up temperature plots for a 70° tilt angle at a 50°C starting temperature with 18W and 70W of heat input. Figure 62 shows a temperature decrease of 0.35°C, just outside of the temperature uncertainty of 0.31°C. All excess temperature measured at start-up except for three data points were greater than the temperature uncertainty.

Figure 62. 18W 50°C 70° tilt start-up.

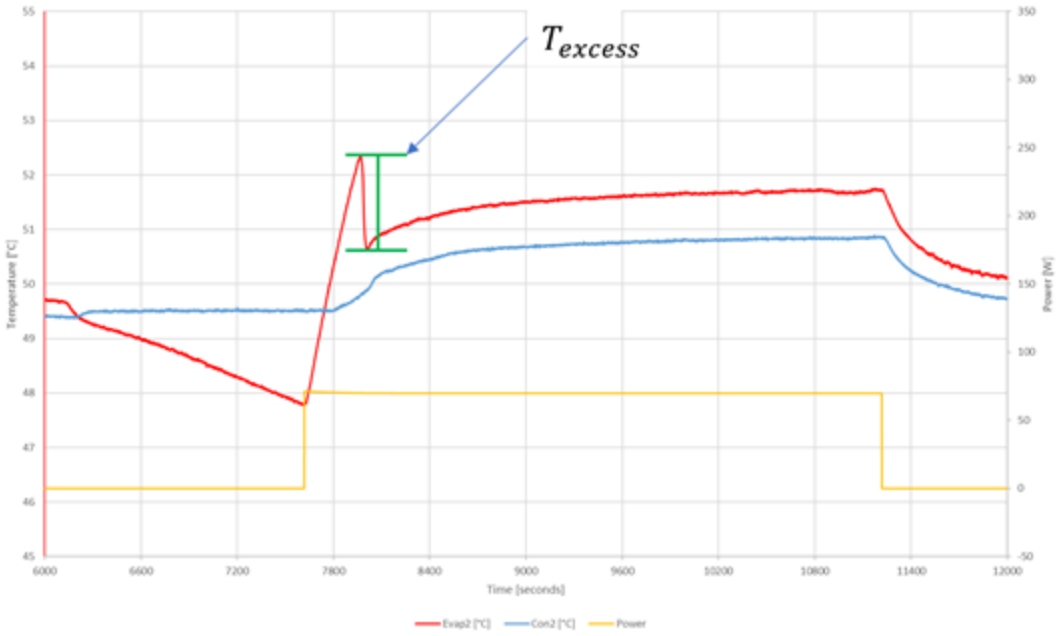

Figure 63. 70W 50°C 70° tilt start-up.

The start-up characteristics of the evaporator were captured in the start-up examples in Figure 62 and Figure 63. Temperature of the evaporator began to elevate once electrical current was delivered to the resistance heating elements. A sudden drop of the evaporator body temperature was recorded as the evaporator's temperature was ramping up. The temperature difference recorded on the evaporator is the excess temperature in Equation 11. The excess temperature measured was different when compared between the 18W and 70W tests. The excess temperature measured in the 70W start-up test was higher than the 14W test. The excess temperature differences measured between the start-up examples conform to the definition of Equation 11. The 70W test yielded a higher heat flux while the 14W test yielded a lower heat flux. Using the same set of fluid properties, solving Equation 11 returned a higher excess temperature for 70W when

compared to 14W. The remaining series of start-up tests were completed from 20°C-60°C in a 10°C initial starting temperature with tilt angles of 0-90° in increments of 10°.

As the tilt angle decreased beyond 60°, the evaporator started boiling immediately once the heating elements were powered on. Start-up power no longer exists as the tilt angle decreased beyond 60°, which could be due to a partially flooded evaporator. The evaporator boiling surface area decreases as the evaporator becomes partially flooded. The heat flux on the internal boiling surface area increased as the internal boiling surface area decreases. This data trend indicates that the tilt angle slightly affects the excess temperature. However, its effect is not as noticeable when compared to adjustments in saturation temperature. The static pressure acting on the boiling surface area decreases as tilt angle decreases. Figure 19 from Section 2.1 shows the amount of fluid column height difference between tilt angles. Equation 11 suggests that the excess temperature slightly lowers as tilt angle decreases. Figure 64 shows the minimum amount of power that was required to initiate boiling inside the evaporator. Figure 65 shows the excess temperatures that were required to initiate boiling inside the evaporator.

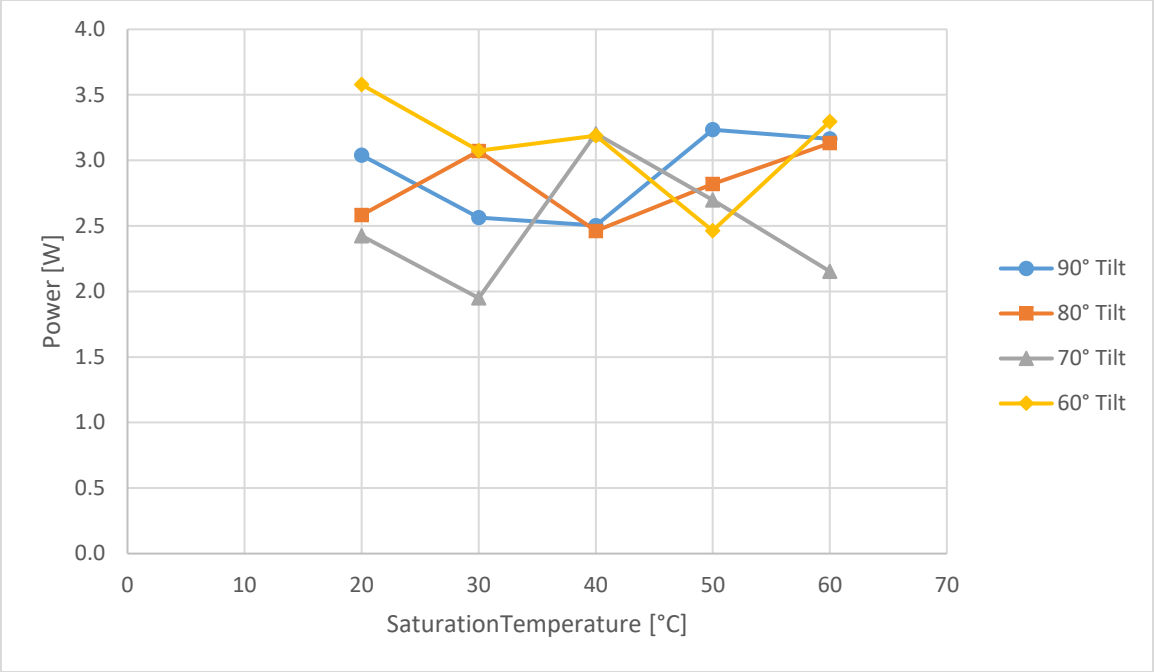

Figure 64. Evaporator start-up power requirement vs. saturation temperature.

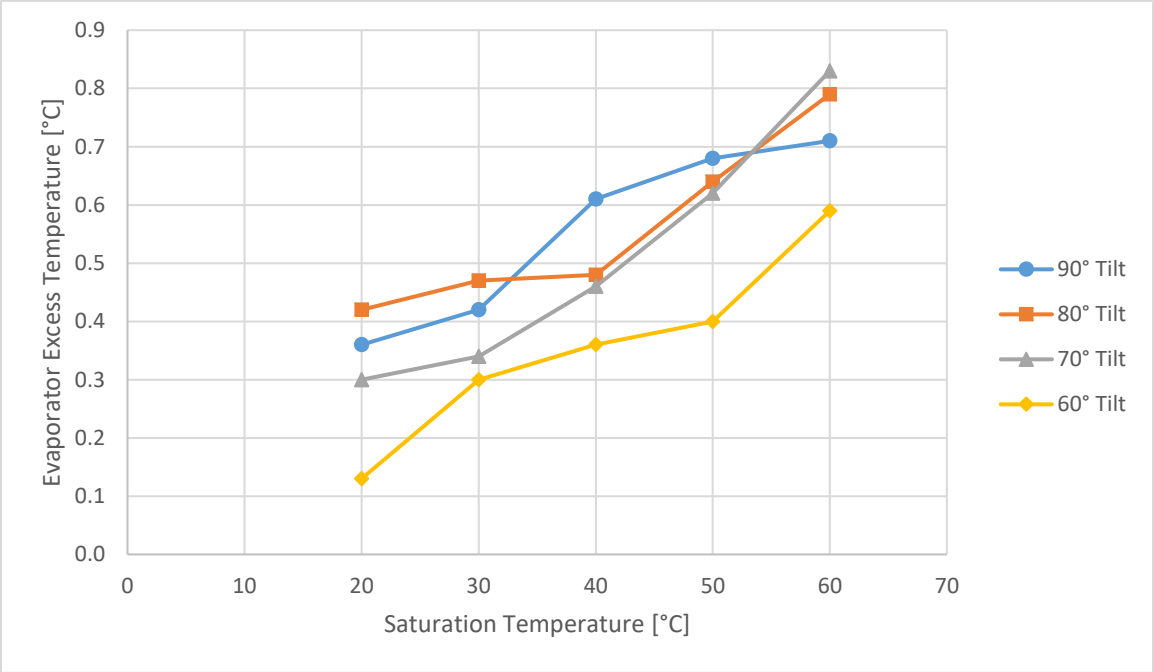

Figure 65. Evaporator excess temperature vs. saturation temperature.

The evaporator excess temperatures found to be required to initiate start-up presented in Figure 65 aligned with the data from Figure 34 generated from Equation 11 using ammonia, the working fluid's properties over the range of operating temperatures. The majority of the variables in Equation 11 decreased as saturation temperature increases. A higher excess temperature on the heated surface was required to maintain a constant heat input requirement presented in Figure 34 to initiate the start-up boiling process inside the evaporator as the saturation temperature increased. Figure 66 shows the data presented in Figure 65 overlaying with the data from Figure 34.

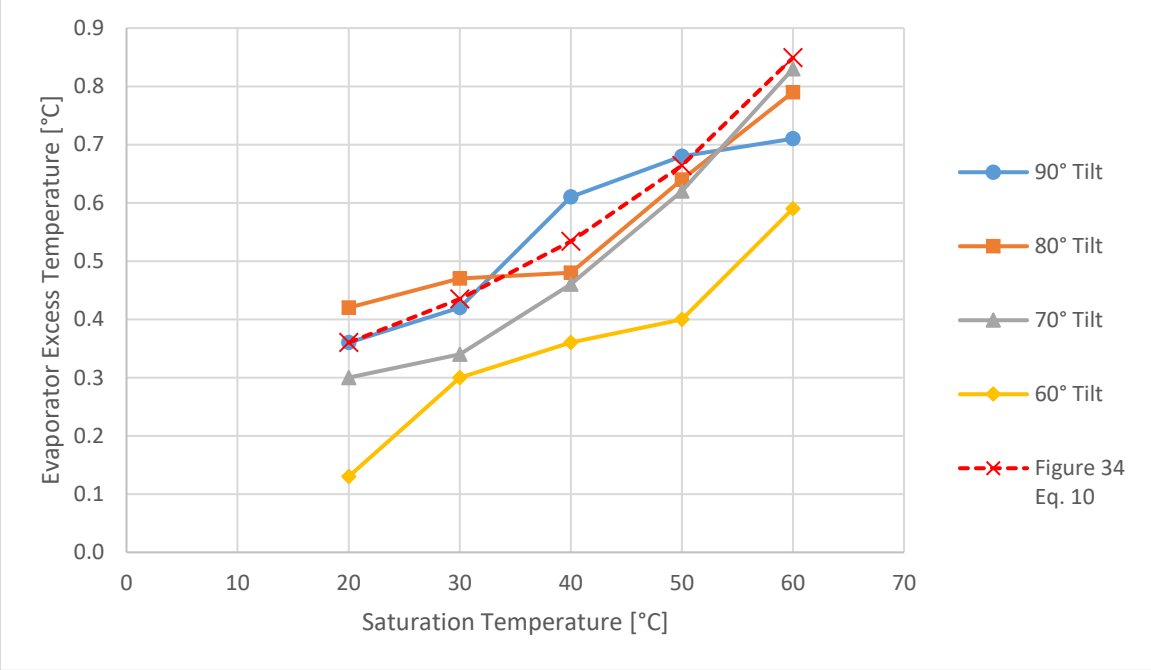

Figure 66. Evaporator excess temperature vs. saturation temperature.

A thermal conductivity test was conducted with a constant heat load of 200W from 0°-90° tilt angle at 20°C saturation temperature to understand the effect of tilt angle on thermal conductivity. Thermal conductivity gradually decreases as the tilt angle decreases from 90° to 0°. The evaporator becomes less flooded as tilt angle decreases

which leads to a smaller boiling surface area. As boiling surface area decreases, heat flux increases which results a higher excess temperature in Equation 11. The evaporator temperature in Equation 7 is directly proportional to the excess temperature in Equation 11. As a result, thermal conductivity decreases as tilt angle decreases. Figure 67 shows the relationship between thermal conductivity and tilt angle.

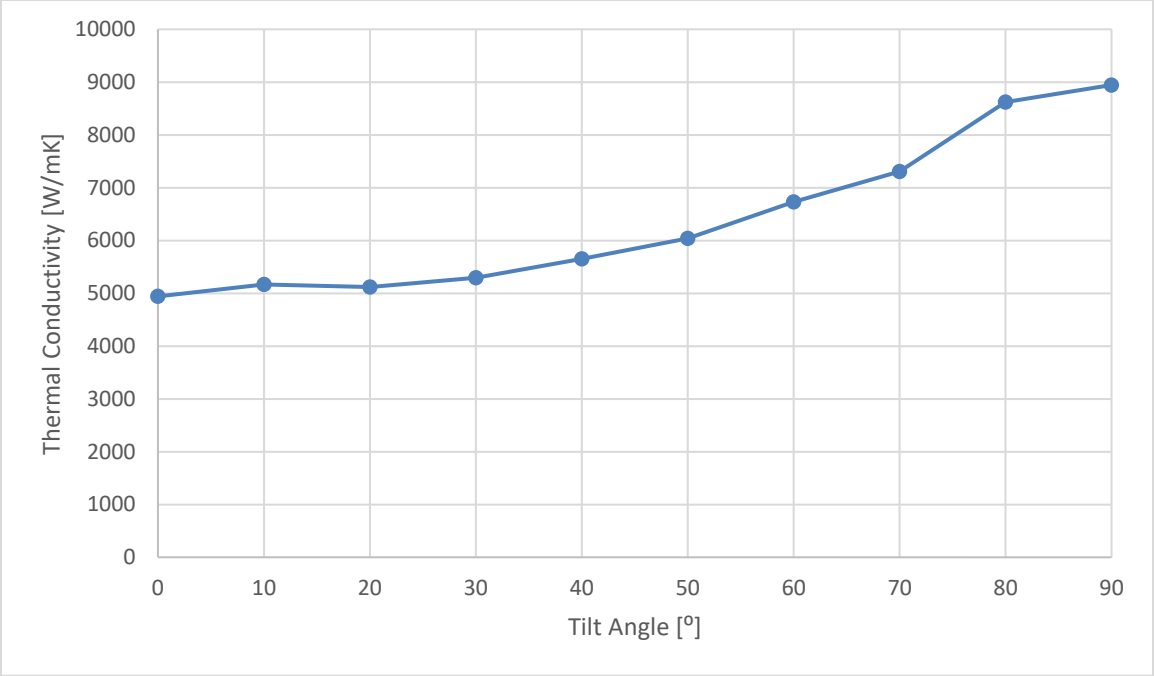

Figure 67. Effective thermal conductivity vs. tilt angle.

5.0 Conclusion and Future Work

Minimum start-up power requirements were found for tilt angles of 90º, 80º, 70º, and 60º at 20ºC, 30ºC, 40ºC, 50ºC, and 60ºC saturation temperatures. Results show the minimum start-up power requirements at different tilt angles and saturation temperature were between 2W and 3.6W. There might be a small correlation between the minimum start-up power and tilt angles and saturation temperatures, but the power difference might be too small for this experiment setup to capture. The excess temperature required to

initiate the start-up boiling process in the evaporator was found to increase as the working fluid's saturation temperature increased. The relationship between the excess temperature and the working fluid's saturation temperature aligns with the nucleate boiling equation. The excess temperature of a heated surface increases as the surface tension of a working fluid decreases if the heat input is to remain constant. The S shaped thermosyphon heat pipe was able to initiate start-up with a smaller excess temperature as the saturation temperature decreased. When the tilt angle decreased to an angle where the evaporator is no longer flooded, no signs of start-up behavior were noticed.

A better heat loss model could help to further improve the results of this experiment. This could better quantify the total amount of heat delivered from the evaporator to the condenser by better insulating the experiment and quantifying heat loss.

References

[1] Çengel, Yunus A., *Heat and Mass Transfer: A Practical Approach*, 3rd ed. Boston: McGraw-Hill, 2007.

[2] J. Qu, H. Wu, and P. Cheng, "Start-up, heat transfer and flow characteristics of silicon-based micro pulsating heat pipes," *International Journal of Heat and Mass Transfer*, vol. 55, no. 21-22, pp. 6109–6120, 2012.

[3] M. Mameli, A. Catarsi, D. Mangini, L. Pietrasanta, N. Michè, M. Marengo, P. D. Marco, and S. Filippeschi, "Start-up in microgravity and local thermodynamic states of a hybrid loop thermosyphon/pulsating heat pipe," *Applied Thermal Engineering*, vol. 158, p. 113771, 2019.

[4] *Space Systems Loral Presentation by Randy Pon, September 2011*

[5] "Programmable DC Power Supply - 62000P: Chroma," *Chroma Systems Solutions, Inc.* [Online]. Available: https://www.chromausa.com/product/programmable-dc-power-supply-62000p/#Overview.

[6] "Thermocouple Types," *Thermocouple Types | Omega Engineering*. [Online]. Available: http://www.omega.com/techref/colorcodes.html.

[7] "34970A Data Acquisition / Data Logger Switch Unit," *34970A Data Acquisition / Data Logger Switch Unit | Keysight (formerly Agilent's Electronic Measurement)*. [Online]. Available: https://www.keysight.com/en/pd-1000001313:epsg:pro-pn-34970A/data-acquisition-data-logger-switch-unit?cc=US&lc=eng.

[8] "Engineering Equation Solver," *Engineering Equation Solver*. F-Chart Software.

[9] "COMSOL Multiphysics," *COMSOL Multiphysics*. COMSOL, Inc.

Appendices

Appendix A – Ammonia PV Calculations

T [°C]	P [kPa]	v_f [m³/kg]	v_g [m³/kg]	v_fg [m³/kg]	ρ_f [kg/m³]	ρ_g [kg/m³]	h_f [kJ/kg]	h_g [kJ/kg]	s_f [kJ/kg]	s_g [kJ/kg]	quality	mass_f [kg]	mass_v [kg]	V_g [m³]	V_f [m³]	V_total [m³]
-30	119.430	0.001475	0.963948	0.962473	677.83	1.03740	206.760	1566.5	0.9446	6.5367	0.003537	0.039261	0.00013937	0.000134	0.00005792	0.000192
-29	125.350	0.001478	0.921234	0.919756	676.58	1.08550	211.230	1568.0	0.9629	6.5199	0.003699	0.039254	0.00014572	0.000134	0.00005802	0.000192
-28	131.510	0.001481	0.880824	0.879344	675.32	1.13530	215.710	1569.4	0.9812	6.5033	0.003865	0.039248	0.00015230	0.000134	0.00005812	0.000192
-27	137.920	0.001484	0.842460	0.840976	674.06	1.18700	220.190	1570.9	0.9994	6.4868	0.004038	0.039241	0.00015912	0.000134	0.00005822	0.000192
-26	144.570	0.001486	0.806127	0.804640	672.80	1.24050	224.680	1572.4	1.0176	6.4705	0.004217	0.039234	0.00016616	0.000134	0.00005831	0.000192
-25	151.470	0.001489	0.771664	0.770175	671.53	1.29590	229.170	1573.8	1.0357	6.4543	0.004402	0.039227	0.00017346	0.000134	0.00005841	0.000192
-24	158.640	0.001492	0.738934	0.737442	670.26	1.35330	233.660	1575.2	1.0537	6.4383	0.004594	0.039219	0.00018101	0.000134	0.00005851	0.000192
-23	166.080	0.001495	0.707914	0.706420	668.98	1.41260	238.170	1576.7	1.0717	6.4224	0.004792	0.039211	0.00018879	0.000134	0.00005861	0.000192
-22	173.790	0.001498	0.678426	0.676928	667.71	1.47400	242.670	1578.1	1.0896	6.4067	0.004996	0.039203	0.00019685	0.000134	0.00005871	0.000192
-21	181.790	0.001501	0.650364	0.648864	666.42	1.53760	247.190	1579.5	1.1075	6.3911	0.005208	0.039195	0.00020519	0.000133	0.00005881	0.000192
-20	190.080	0.001503	0.623714	0.622210	665.14	1.60330	251.710	1580.8	1.1253	6.3757	0.005426	0.039186	0.00021380	0.000133	0.00005891	0.000192
-19	198.670	0.001506	0.598408	0.596902	663.85	1.67110	256.230	1582.2	1.1431	6.3604	0.005652	0.039177	0.00022267	0.000133	0.00005902	0.000192
-18	207.560	0.001509	0.574284	0.572774	662.55	1.74130	260.760	1583.5	1.1609	6.3452	0.005884	0.039168	0.00023185	0.000133	0.00005912	0.000192
-17	216.770	0.001512	0.551329	0.549816	661.25	1.81380	265.290	1584.9	1.1785	6.3302	0.006125	0.039159	0.00024132	0.000133	0.00005922	0.000192
-16	226.300	0.001515	0.529493	0.527977	659.95	1.88860	269.830	1586.2	1.1962	6.3153	0.006372	0.039149	0.00025108	0.000133	0.00005932	0.000192
-15	236.170	0.001518	0.508673	0.507155	658.65	1.96590	274.370	1587.5	1.2137	6.3005	0.006628	0.039139	0.00026115	0.000133	0.00005942	0.000192
-14	246.370	0.001521	0.488854	0.487333	657.34	2.04560	278.920	1588.8	1.2313	6.2859	0.006892	0.039128	0.00027153	0.000133	0.00005953	0.000192
-13	256.910	0.001524	0.469947	0.468423	656.02	2.12790	283.470	1590.1	1.2487	6.2713	0.007163	0.039118	0.00028223	0.000133	0.00005963	0.000192
-12	267.820	0.001527	0.451916	0.450389	654.70	2.21280	288.030	1591.4	1.2662	6.2569	0.007443	0.039107	0.00029327	0.000133	0.00005973	0.000192
-11	279.080	0.001531	0.434726	0.433195	653.38	2.30030	292.600	1592.6	1.2835	6.2426	0.007732	0.039095	0.00030463	0.000132	0.00005984	0.000192
-10	290.710	0.001534	0.418305	0.416771	652.06	2.39060	297.160	1593.9	1.3009	6.2285	0.008029	0.039084	0.00031634	0.000132	0.00005994	0.000192
-9	302.730	0.001537	0.402625	0.401088	650.73	2.48370	301.740	1595.1	1.3181	6.2144	0.008335	0.039072	0.00032840	0.000132	0.00006004	0.000192
-8	315.130	0.00154	0.387672	0.386132	649.39	2.57950	306.320	1596.3	1.3354	6.2004	0.00865	0.039059	0.00034079	0.000132	0.00006015	0.000192
-7	327.930	0.001543	0.373371	0.371828	648.06	2.67830	310.900	1597.5	1.3526	6.1866	0.008974	0.039046	0.00035357	0.000132	0.00006025	0.000192
-6	341.140	0.001546	0.359699	0.358153	646.71	2.78010	315.490	1598.7	1.3697	6.1729	0.009307	0.039033	0.00036672	0.000132	0.00006036	0.000192
-5	354.760	0.001549	0.346632	0.345083	645.37	2.88490	320.090	1599.8	1.3868	6.1592	0.009651	0.03902	0.00038024	0.000132	0.00006046	0.000192
-4	368.800	0.001553	0.334135	0.332583	644.02	2.99280	324.690	1601.0	1.4038	6.1457	0.010004	0.039006	0.00039415	0.000132	0.00006057	0.000192
-3	383.270	0.001556	0.322186	0.320630	642.66	3.10380	329.300	1602.1	1.4209	6.1323	0.010366	0.038992	0.00040843	0.000132	0.00006067	0.000192
-2	398.190	0.001559	0.310742	0.309183	641.30	3.21810	333.910	1603.2	1.4378	6.1190	0.010739	0.038977	0.00042314	0.000131	0.00006078	0.000192
-1	413.560	0.001563	0.299787	0.298225	639.94	3.33570	338.530	1604.3	1.4547	6.1058	0.011123	0.038962	0.00043825	0.000131	0.00006088	0.000192
0	429.380	0.001566	0.289293	0.287727	638.57	3.45670	343.150	1605.4	1.4716	6.0926	0.011517	0.038946	0.00045378	0.000131	0.00006099	0.000192
1	445.680	0.001569	0.279244	0.277674	637.20	3.58110	347.780	1606.5	1.4884	6.0796	0.011922	0.03893	0.00046973	0.000131	0.00006110	0.000192
2	462.460	0.001573	0.269614	0.268042	635.82	3.70900	352.420	1607.5	1.5052	6.0667	0.012338	0.038914	0.00048611	0.000131	0.00006120	0.000192
3	479.720	0.001576	0.260383	0.258807	634.44	3.84050	357.060	1608.5	1.5219	6.0538	0.012765	0.038897	0.00050293	0.000131	0.00006131	0.000192
4	497.480	0.00158	0.251528	0.249948	633.06	3.97570	361.710	1609.6	1.5386	6.0410	0.013203	0.03888	0.00052021	0.000131	0.00006142	0.000192
5	515.750	0.001583	0.243037	0.241454	631.66	4.11460	366.360	1610.5	1.5553	6.0284	0.013653	0.038862	0.00053794	0.000131	0.00006152	0.000192
6	534.530	0.001587	0.234891	0.233304	630.27	4.25730	371.020	1611.5	1.5719	6.0158	0.014115	0.038844	0.00055615	0.000131	0.00006163	0.000192
7	553.850	0.00159	0.227071	0.225481	628.87	4.40390	375.690	1612.5	1.5885	6.0033	0.014589	0.038825	0.00057482	0.000131	0.00006174	0.000192
8	573.700	0.001594	0.219563	0.217969	627.46	4.55450	380.360	1613.4	1.6050	5.9908	0.015076	0.038806	0.00059399	0.00013	0.00006185	0.000192
9	594.090	0.001597	0.212350	0.210753	626.05	4.70920	385.040	1614.4	1.6215	5.9785	0.015575	0.038786	0.00061366	0.00013	0.00006195	0.000192

T [°C]	P [kPa]	v_f [m³/kg]	v_g [m³/kg]	v_fg [m³/kg]	ρ_f [kg/m³]	ρ_g [kg/m³]	h_f [kJ/kg]	h_g [kJ/kg]	s_f [kJ/kg]	s_g [kJ/kg]	quality	mass_f [kg]	mass_v [kg]	V_g [m³]	V_f [m³]	V_total [m³]
10	615.050	0.001601	0.205427	0.203826	624.64	4.86790	389.720	1615.3	1.6380	5.9662	0.016087	0.038766	0.00063381	0.00013	0.00006206	0.000192
11	636.570	0.001605	0.198772	0.197167	623.22	5.03090	394.410	1616.2	1.6544	5.9540	0.016611	0.038746	0.00065449	0.00013	0.00006217	0.000192
12	658.660	0.001608	0.192371	0.190762	621.79	5.19830	399.110	1617.0	1.6708	5.9419	0.01715	0.038724	0.00067570	0.00013	0.00006228	0.000192
13	681.350	0.001612	0.186220	0.184608	620.36	5.37000	403.810	1617.9	1.6871	5.9299	0.017701	0.038703	0.00069744	0.00013	0.00006239	0.000192
14	704.630	0.001616	0.180307	0.178691	618.93	5.54610	408.520	1618.7	1.7034	5.9179	0.018267	0.03868	0.00071971	0.00013	0.00006250	0.000192
15	728.520	0.001619	0.174615	0.172995	617.49	5.72690	413.240	1619.5	1.7197	5.9060	0.018846	0.038657	0.00074255	0.00013	0.00006260	0.000192
16	753.030	0.001623	0.169139	0.167516	616.04	5.91230	417.970	1620.3	1.7359	5.8941	0.01944	0.038634	0.00076594	0.00013	0.00006271	0.000192
17	778.170	0.001627	0.163867	0.162240	614.59	6.10250	422.700	1621.1	1.7521	5.8824	0.020049	0.03861	0.00078992	0.000129	0.00006282	0.000192
18	803.950	0.001631	0.158793	0.157162	613.13	6.29750	427.440	1621.9	1.7682	5.8707	0.020672	0.038586	0.00081447	0.000129	0.00006293	0.000192
19	830.380	0.001635	0.153905	0.152270	611.67	6.49750	432.180	1622.6	1.7844	5.8590	0.02131	0.03856	0.00083963	0.000129	0.00006304	0.000192
20	857.480	0.001639	0.149198	0.147559	610.20	6.70250	436.940	1623.3	1.8005	5.8475	0.021964	0.038535	0.00086538	0.000129	0.00006315	0.000192
21	885.240	0.001643	0.144661	0.143018	608.72	6.91270	441.700	1624.0	1.8165	5.8359	0.022633	0.038508	0.00089176	0.000129	0.00006326	0.000192
22	913.690	0.001647	0.140290	0.138643	607.24	7.12810	446.470	1624.7	1.8326	5.8245	0.023319	0.038481	0.00091876	0.000129	0.00006337	0.000192
23	942.830	0.001651	0.136077	0.134426	605.76	7.34880	451.240	1625.3	1.8485	5.8131	0.024021	0.038454	0.00094641	0.000129	0.00006348	0.000192
24	972.680	0.001655	0.132011	0.130357	604.26	7.57510	456.030	1626.0	1.8645	5.8017	0.024739	0.038425	0.00097471	0.000129	0.00006359	0.000192
25	1003.200	0.001659	0.128092	0.126433	602.76	7.80690	460.820	1626.6	1.8804	5.7904	0.025474	0.038396	0.00100368	0.000129	0.00006370	0.000192
26	1034.500	0.001663	0.124312	0.122648	601.26	8.04430	465.620	1627.2	1.8963	5.7792	0.026226	0.038367	0.00103332	0.000128	0.00006381	0.000192
27	1066.600	0.001667	0.120662	0.118995	599.75	8.28760	470.430	1627.7	1.9122	5.7680	0.026996	0.038336	0.00106366	0.000128	0.00006392	0.000192
28	1099.300	0.001672	0.117140	0.115468	598.23	8.53680	475.250	1628.3	1.9281	5.7569	0.027784	0.038305	0.00109470	0.000128	0.00006403	0.000192
29	1132.900	0.001676	0.113740	0.112064	596.70	8.79200	480.080	1628.8	1.9439	5.7458	0.02859	0.038274	0.00112645	0.000128	0.00006414	0.000192
30	1167.200	0.00168	0.110457	0.108777	595.17	9.05330	484.910	1629.3	1.9597	5.7347	0.029414	0.038241	0.00115893	0.000128	0.00006425	0.000192
31	1202.300	0.001685	0.107286	0.105601	593.63	9.32090	489.760	1629.8	1.9754	5.7237	0.030258	0.038208	0.00119215	0.000128	0.00006436	0.000192
32	1238.200	0.001689	0.104221	0.102532	592.08	9.59500	494.610	1630.3	1.9911	5.7128	0.03112	0.038174	0.00122614	0.000128	0.00006447	0.000192
33	1274.900	0.001693	0.101261	0.099567	590.53	9.87550	499.470	1630.7	2.0069	5.7019	0.032003	0.038139	0.00126090	0.000128	0.00006458	0.000192
34	1312.400	0.001698	0.098396	0.096698	588.97	10.16300	504.340	1631.1	2.0225	5.6910	0.032906	0.038104	0.00129648	0.000128	0.00006470	0.000192
35	1350.800	0.001702	0.095630	0.093927	587.40	10.45700	509.230	1631.5	2.0382	5.6801	0.033828	0.038067	0.00133283	0.000127	0.00006481	0.000192
36	1390.000	0.001707	0.092954	0.091247	585.82	10.75800	514.120	1631.9	2.0538	5.6693	0.034771	0.03803	0.00136999	0.000127	0.00006492	0.000192
37	1430.000	0.001712	0.090367	0.088655	584.24	11.06600	519.020	1632.2	2.0694	5.6586	0.035736	0.037992	0.00140799	0.000127	0.00006503	0.000192
38	1470.900	0.001716	0.087866	0.086149	582.65	11.38100	523.930	1632.5	2.0850	5.6479	0.036721	0.037953	0.00144681	0.000127	0.00006514	0.000192
39	1512.700	0.001721	0.085448	0.083727	581.05	11.70300	528.860	1632.8	2.1006	5.6372	0.037727	0.037914	0.00148644	0.000127	0.00006525	0.000192
40	1555.400	0.001726	0.083098	0.081372	579.44	12.03400	533.790	1633.1	2.1161	5.6265	0.03876	0.037873	0.00152715	0.000127	0.00006536	0.000192
41	1599.000	0.001731	0.080834	0.079104	577.82	12.37100	538.740	1633.3	2.1317	5.6159	0.039811	0.037831	0.00156853	0.000127	0.00006547	0.000192
42	1643.500	0.001736	0.078635	0.076899	576.20	12.71700	543.690	1633.5	2.1472	5.6053	0.040888	0.037789	0.00161100	0.000127	0.00006558	0.000192
43	1689.000	0.00174	0.076505	0.074765	574.56	13.07100	548.660	1633.7	2.1627	5.5947	0.041989	0.037746	0.00165439	0.000127	0.00006569	0.000192
44	1735.300	0.001745	0.074449	0.072704	572.92	13.43200	553.640	1633.9	2.1781	5.5841	0.043111	0.037701	0.00169859	0.000126	0.00006581	0.000192
45	1782.700	0.00175	0.072448	0.070698	571.27	13.80300	558.630	1634.0	2.1936	5.5736	0.044263	0.037656	0.00174398	0.000126	0.00006592	0.000192
46	1831.000	0.001756	0.070517	0.068761	569.61	14.18100	563.630	1634.1	2.2090	5.5631	0.045436	0.03761	0.00179016	0.000126	0.00006603	0.000192
47	1880.200	0.001761	0.068639	0.066878	567.94	14.56900	568.650	1634.2	2.2244	5.5526	0.046638	0.037562	0.00183753	0.000126	0.00006614	0.000192
48	1930.500	0.001766	0.066823	0.065057	566.25	14.96500	573.680	1634.2	2.2398	5.5422	0.047863	0.037514	0.00188580	0.000126	0.00006625	0.000192
49	1981.800	0.001771	0.065058	0.063286	564.56	15.37100	578.720	1634.2	2.2552	5.5317	0.049118	0.037465	0.00193526	0.000126	0.00006636	0.000192

T [°C]	P [kPa]	v_f [m³/kg]	v_g [m³/kg]	v_fg [m³/kg]	ρ_f [kg/m³]	ρ_g [kg/m³]	h_f [kJ/kg]	h_g [kJ/kg]	s_f [kJ/kg]	s_g [kJ/kg]	quality	mass_f [kg]	mass_v [kg]	V_g [m³]	V_f [m³]	V_total [m³]
50	2034.000	0.001777	0.063351	0.061575	562.86	15.78500	583.770	1634.2	2.2706	5.5213	0.050397	0.037414	0.00198563	0.000126	0.00006647	0.000192
51	2087.300	0.001782	0.061694	0.059912	561.15	16.20900	588.840	1634.2	2.2860	5.5109	0.051705	0.037363	0.00203717	0.000126	0.00006658	0.000192
52	2141.700	0.001788	0.060085	0.058298	559.43	16.64300	593.920	1634.1	2.3013	5.5005	0.053043	0.03731	0.00208988	0.000126	0.00006669	0.000192
53	2197.100	0.001793	0.058524	0.056731	557.70	17.08700	599.020	1634.0	2.3167	5.4901	0.05441	0.037256	0.00214375	0.000125	0.00006680	0.000192
54	2253.600	0.001799	0.057009	0.055211	555.95	17.54100	604.130	1633.9	2.3320	5.4797	0.055806	0.037201	0.00219875	0.000125	0.00006691	0.000192
55	2311.100	0.001804	0.055537	0.053733	554.20	18.00600	609.260	1633.7	2.3473	5.4693	0.057235	0.037145	0.00225506	0.000125	0.00006702	0.000192
56	2369.800	0.00181	0.054110	0.052299	552.43	18.48100	614.400	1633.5	2.3627	5.4589	0.058693	0.037087	0.00231251	0.000125	0.00006714	0.000192
57	2429.500	0.001816	0.052723	0.050907	550.65	18.96700	619.560	1633.3	2.3780	5.4486	0.060183	0.037029	0.00237122	0.000125	0.00006725	0.000192
58	2490.400	0.001822	0.051377	0.049555	548.86	19.46400	624.730	1633.0	2.3933	5.4382	0.061706	0.036969	0.00243122	0.000125	0.00006736	0.000192
59	2552.400	0.001828	0.050068	0.048240	547.06	19.97300	629.920	1632.7	2.4086	5.4278	0.063264	0.036907	0.00249261	0.000125	0.00006746	0.000192
60	2615.600	0.001834	0.048797	0.046963	545.24	20.49300	635.120	1632.4	2.4239	5.4174	0.064854	0.036845	0.00255525	0.000125	0.00006758	0.000192
61	2679.900	0.00184	0.047562	0.045722	543.41	21.02500	640.350	1632.1	2.4392	5.4071	0.066479	0.036781	0.00261927	0.000125	0.00006769	0.000192
62	2745.400	0.001846	0.046361	0.044514	541.57	21.57000	645.590	1631.7	2.4545	5.3967	0.068143	0.036715	0.00268482	0.000124	0.00006779	0.000192
63	2812.100	0.001853	0.045194	0.043341	539.72	22.12700	650.840	1631.2	2.4698	5.3863	0.069841	0.036648	0.00275175	0.000124	0.00006790	0.000192
64	2880.000	0.001859	0.044059	0.042199	537.85	22.69700	656.120	1630.8	2.4851	5.3759	0.071578	0.03658	0.00282017	0.000124	0.00006801	0.000192
65	2949.100	0.001866	0.042955	0.041090	535.96	23.28000	661.420	1630.2	2.5004	5.3655	0.073352	0.03651	0.00289006	0.000124	0.00006812	0.000192
66	3019.500	0.001872	0.041881	0.040009	534.06	23.87700	666.730	1629.7	2.5157	5.3550	0.075167	0.036438	0.00296158	0.000124	0.00006823	0.000192
67	3091.100	0.001879	0.040836	0.038957	532.15	24.48800	672.070	1629.1	2.5310	5.3446	0.077024	0.036365	0.00303474	0.000124	0.00006834	0.000192
68	3163.900	0.001886	0.039820	0.037934	530.22	25.11300	677.420	1628.5	2.5463	5.3341	0.078921	0.036291	0.00310949	0.000124	0.00006844	0.000192
69	3238.100	0.001893	0.038830	0.036937	528.27	25.75300	682.800	1627.8	2.5617	5.3236	0.080862	0.036214	0.00318595	0.000124	0.00006855	0.000192
70	3313.500	0.0019	0.037869	0.035969	526.31	26.40700	688.200	1627.1	2.5770	5.3131	0.082844	0.036136	0.00326403	0.000124	0.00006866	0.000192
71	3390.200	0.001907	0.036930	0.035023	524.33	27.07800	693.620	1626.3	2.5923	5.3026	0.084875	0.036056	0.00334409	0.000123	0.00006877	0.000192
72	3468.200	0.001914	0.036018	0.034103	522.33	27.76400	699.060	1625.5	2.6077	5.2920	0.08695	0.035974	0.00342584	0.000123	0.00006887	0.000192
73	3547.600	0.001922	0.035128	0.033207	520.32	28.46700	704.530	1624.7	2.6231	5.2814	0.089076	0.03589	0.00350960	0.000123	0.00006898	0.000192
74	3628.400	0.001929	0.034263	0.032334	518.28	29.18600	710.020	1623.8	2.6385	5.2707	0.091247	0.035805	0.00359513	0.000123	0.00006908	0.000192
75	3710.500	0.001937	0.033419	0.031482	516.23	29.92300	715.530	1622.9	2.6539	5.2601	0.093472	0.035717	0.00368279	0.000123	0.00006919	0.000192
76	3793.900	0.001945	0.032597	0.030652	514.16	30.67800	721.070	1621.9	2.6693	5.2493	0.095749	0.035627	0.00377252	0.000123	0.00006929	0.000192
77	3878.800	0.001953	0.031795	0.029843	512.07	31.45100	726.640	1620.9	2.6847	5.2386	0.098079	0.035536	0.00386432	0.000123	0.00006940	0.000192
78	3965.100	0.001961	0.031014	0.029053	509.96	32.24400	732.230	1619.8	2.7002	5.2278	0.100468	0.035442	0.00395844	0.000123	0.00006950	0.000192
79	4052.800	0.001969	0.030252	0.028283	507.83	33.05600	737.850	1618.6	2.7157	5.2169	0.102913	0.035345	0.00405476	0.000123	0.00006960	0.000192
80	4142.000	0.001978	0.029509	0.027531	505.67	33.88800	743.500	1617.5	2.7312	5.2060	0.105415	0.035247	0.00415335	0.000123	0.00006970	0.000192
81	4232.600	0.001986	0.028784	0.026798	503.49	34.74100	749.180	1616.2	2.7468	5.1950	0.107979	0.035146	0.00425438	0.000122	0.00006980	0.000192
82	4324.700	0.001995	0.028078	0.026083	501.29	35.61500	754.880	1614.9	2.7623	5.1840	0.110605	0.035042	0.00435785	0.000122	0.00006990	0.000192
83	4418.300	0.002004	0.027388	0.025385	499.07	36.51200	760.620	1613.6	2.7780	5.1729	0.1133	0.034936	0.00446402	0.000122	0.00007000	0.000192
84	4513.400	0.002013	0.026715	0.024702	496.82	37.43200	766.390	1612.2	2.7936	5.1617	0.116062	0.034827	0.00457284	0.000122	0.00007010	0.000192
85	4610.000	0.002022	0.026058	0.024036	494.54	38.37600	772.200	1610.7	2.8093	5.1504	0.118894	0.034716	0.00468442	0.000122	0.00007020	0.000192
86	4708.200	0.002032	0.025417	0.023385	492.24	39.34400	778.040	1609.1	2.8250	5.1391	0.121797	0.034601	0.00479881	0.000122	0.00007029	0.000192
87	4807.900	0.002041	0.024791	0.022749	489.91	40.33800	783.910	1607.5	2.8408	5.1277	0.124778	0.034484	0.00491624	0.000122	0.00007039	0.000192
88	4909.300	0.002051	0.024179	0.022128	487.56	41.35900	789.820	1605.9	2.8566	5.1162	0.127839	0.034363	0.00503687	0.000122	0.00007048	0.000192
89	5012.200	0.002061	0.023581	0.021520	485.17	42.40700	795.770	1604.1	2.8725	5.1046	0.13098	0.034239	0.00516059	0.000122	0.00007057	0.000192

T [°C]	P [kPa]	v_f [m³/kg]	v_g [m³/kg]	v_fg [m³/kg]	ρ_f [kg/m³]	ρ_g [kg/m³]	h_f [kJ/kg]	h_g [kJ/kg]	s_f [kJ/kg]	s_g [kJ/kg]	quality	mass_f [kg]	mass_v [kg]	V_g [m³]	V_f [m³]	V_total [m³]
90	5116.70	0.002071	0.022997	0.020925	482.75	43.484	801.760	1602.3	2.8884	5.0929	0.134206	0.034112	0.00528772	0.000122	0.00007066	0.000192
91	5222.90	0.002082	0.022427	0.020345	480.31	44.590	807.790	1600.5	2.9043	5.0811	0.137521	0.033982	0.00541833	0.000122	0.00007075	0.000192
92	5330.70	0.002093	0.021868	0.019776	477.82	45.728	813.860	1598.5	2.9204	5.0692	0.140929	0.033847	0.00555261	0.000121	0.00007084	0.000192
93	5440.20	0.002104	0.021323	0.019219	475.31	46.898	819.970	1596.5	2.9365	5.0572	0.144436	0.033709	0.00569077	0.000121	0.00007092	0.000192
94	5551.40	0.002115	0.020790	0.018674	472.76	48.101	826.130	1594.4	2.9526	5.0450	0.14804	0.033567	0.00583279	0.000121	0.00007100	0.000192
95	5664.30	0.002127	0.020268	0.018141	470.17	49.340	832.340	1592.2	2.9689	5.0327	0.151754	0.033421	0.00597909	0.000121	0.00007108	0.000192
96	5779.00	0.002139	0.019757	0.017618	467.55	50.615	838.600	1589.9	2.9852	5.0203	0.155577	0.03327	0.00612974	0.000121	0.00007116	0.000192
97	5895.40	0.002151	0.019257	0.017106	464.88	51.928	844.910	1587.5	3.0016	5.0078	0.159514	0.033115	0.00628486	0.000121	0.00007123	0.000192
98	6013.50	0.002164	0.018768	0.016604	462.18	53.282	851.270	1585.0	3.0180	4.9950	0.163579	0.032955	0.00644503	0.000121	0.00007130	0.000192
99	6133.50	0.002177	0.018289	0.016113	459.43	54.677	857.680	1582.5	3.0346	4.9821	0.167768	0.03279	0.00661007	0.000121	0.00007137	0.000192
100	6255.30	0.00219	0.017820	0.015630	456.63	56.117	864.160	1579.8	3.0513	4.9691	0.172095	0.032619	0.00678055	0.000121	0.00007144	0.000192
101	6378.90	0.002204	0.017360	0.015157	453.79	57.603	870.690	1577.0	3.0680	4.9558	0.176566	0.032443	0.00695671	0.000121	0.00007149	0.000192
102	6504.40	0.002218	0.016910	0.014692	450.90	59.138	877.290	1574.1	3.0849	4.9424	0.18119	0.032261	0.00713889	0.000121	0.00007155	0.000192
103	6631.80	0.002232	0.016468	0.014236	447.95	60.724	883.960	1571.1	3.1019	4.9287	0.185971	0.032073	0.00732727	0.000121	0.00007160	0.000192
104	6761.00	0.002247	0.016035	0.013787	444.95	62.365	890.700	1568.0	3.1190	4.9148	0.190927	0.031877	0.00752254	0.000121	0.00007164	0.000192
105	6892.30	0.002263	0.015610	0.013347	441.90	64.063	897.510	1564.7	3.1363	4.9007	0.196067	0.031675	0.00772503	0.000121	0.00007168	0.000192
106	7025.50	0.002279	0.015192	0.012913	438.78	65.822	904.400	1561.3	3.1537	4.8863	0.201399	0.031465	0.00793511	0.000121	0.00007171	0.000192
107	7160.60	0.002296	0.014783	0.012487	435.59	67.646	911.370	1557.8	3.1712	4.8716	0.206938	0.031247	0.00815337	0.000121	0.00007173	0.000192
108	7297.80	0.002313	0.014380	0.012067	432.34	69.539	918.430	1554.1	3.1889	4.8567	0.212705	0.031019	0.00838058	0.000121	0.00007175	0.000192
109	7437.00	0.002331	0.013985	0.011654	429.01	71.505	925.580	1550.2	3.2068	4.8414	0.218709	0.030783	0.00861712	0.000121	0.00007175	0.000192
110	7578.30	0.00235	0.013596	0.011247	425.61	73.550	932.840	1546.2	3.2249	4.8258	0.224977	0.030536	0.00886408	0.000121	0.00007175	0.000192
111	7721.70	0.002369	0.013214	0.010845	422.12	75.679	940.200	1542.0	3.2432	4.8099	0.231523	0.030278	0.00912201	0.000121	0.00007173	0.000192
112	7867.30	0.002389	0.012837	0.010448	418.54	77.899	947.680	1537.6	3.2618	4.7935	0.238378	0.030008	0.00939207	0.000121	0.00007170	0.000192
113	8015.00	0.00241	0.012466	0.010056	414.86	80.217	955.280	1533.0	3.2805	4.7768	0.245566	0.029725	0.00967530	0.000121	0.00007165	0.000192
114	8164.90	0.002433	0.012100	0.009668	411.08	82.642	963.010	1528.2	3.2996	4.7595	0.253128	0.029427	0.00997323	0.000121	0.00007158	0.000192
115	8317.00	0.002456	0.011740	0.009284	407.18	85.182	970.890	1523.1	3.3190	4.7418	0.261091	0.029113	0.01028700	0.000121	0.00007150	0.000192
116	8471.40	0.00248	0.011383	0.008903	403.15	87.849	978.930	1517.8	3.3387	4.7235	0.269506	0.028781	0.01061853	0.000121	0.00007139	0.000192
117	8628.10	0.002506	0.011031	0.008525	398.99	90.654	987.150	1512.2	3.3588	4.7046	0.278425	0.02843	0.01096994	0.000121	0.00007126	0.000192
118	8787.20	0.002534	0.010682	0.008148	394.67	93.614	995.560	1506.3	3.3793	4.6850	0.287914	0.028056	0.01134379	0.000121	0.00007109	0.000192
119	8948.60	0.002563	0.010336	0.007774	390.18	96.745	1004.200	1500.0	3.4003	4.6647	0.298047	0.027657	0.01174305	0.000121	0.00007088	0.000192
120	9112.50	0.002594	0.009993	0.007399	385.49	100.070	1013.100	1493.4	3.4218	4.6435	0.308924	0.027228	0.01217159	0.000122	0.00007063	0.000192
121	9278.90	0.002628	0.009652	0.007024	380.57	103.610	1022.200	1486.3	3.4440	4.6214	0.32064	0.026767	0.01263323	0.000122	0.00007033	0.000192
122	9447.80	0.002664	0.009311	0.006647	375.40	107.400	1031.700	1478.7	3.4669	4.5982	0.333371	0.026265	0.01313482	0.000122	0.00006997	0.000192
123	9619.20	0.002703	0.008970	0.006267	369.93	111.480	1041.600	1470.6	3.4907	4.5737	0.347308	0.025716	0.01368395	0.000123	0.00006952	0.000192
124	9793.40	0.002747	0.008628	0.005881	364.08	115.900	1051.900	1461.8	3.5156	4.5477	0.362689	0.02511	0.01428995	0.000123	0.00006897	0.000192
125	9970.20	0.002795	0.008283	0.005488	357.80	120.730	1062.800	1452.3	3.5417	4.5199	0.379903	0.024432	0.01496817	0.000124	0.00006828	0.000192
126	10150.00	0.002849	0.007933	0.005083	350.95	126.060	1074.400	1441.8	3.5696	4.4899	0.399422	0.023663	0.01573721	0.000125	0.00006742	0.000192
127	10332.00	0.002912	0.007574	0.004662	343.37	132.030	1087.000	1430.1	3.5996	4.4570	0.422051	0.022771	0.01662881	0.000126	0.00006632	0.000192
128	10518.00	0.002987	0.007202	0.004215	334.79	138.850	1100.800	1416.8	3.6327	4.4205	0.449067	0.021707	0.01769325	0.000127	0.00006484	0.000192
129	10706.00	0.003079	0.006809	0.003729	324.74	146.870	1116.400	1401.3	3.6702	4.3787	0.482767	0.020379	0.01902102	0.00013	0.00006275	0.000192

Appendix B – Nucleate Boiling Calculations

T [°C]	Pressure [kPa]	σ [N/m]	μ_vapor [kg/m s]	μ_liquid [kg/m s]	ρ_g [kg/m³]	ρ_f [kg/m³]	h_f [kJ/kg]	h_g [kJ/kg]	h_fg [kJ/kg]	Pr_l	T_s [°C]	T_excess [°C]	C_pl	q [W/m^2]
-30	119.4	0.03341	8.31E-06	0.000263	1.037	677.8	206.76	1566.5	1359.74	1.017	-29.832	0.168	2.326	0.179
-20	190.1	0.03118	8.67E-06	0.000236	1.603	665.1	251.71	1580.8	1329.09	1.043	-19.810	0.190	2.425	0.179
-10	290.8	0.02896	9.03E-06	0.000212	2.391	652.1	297.16	1593.9	1296.74	1.074	-9.782	0.218	2.542	0.178
0	429.6	0.02676	9.41E-06	0.00019	3.458	638.6	343.15	1605.4	1262.25	1.110	0.254	0.254	2.680	0.177
10	615.3	0.02457	9.78E-06	0.00017	4.87	624.6	389.72	1615.3	1225.58	1.151	10.300	0.300	2.842	0.177
20	857.8	0.0224	1.02E-05	0.000152	6.705	610.2	436.94	1623.3	1186.36	1.198	20.360	0.360	3.030	0.178
30	1167	0.02024	1.06E-05	0.000136	9.055	595.2	484.91	1629.3	1144.39	1.251	30.435	0.435	3.250	0.178
40	1555	0.0181	0.000011	0.000122	12.03	579.4	533.79	1633.1	1099.31	1.312	40.534	0.534	3.510	0.178
50	2033	0.01598	1.14E-05	0.00011	15.78	562.9	583.77	1634.2	1050.43	1.382	50.664	0.664	3.822	0.178
60	2614	0.01389	1.19E-05	9.85E-05	20.48	545.2	635.12	1632.4	997.28	1.467	60.849	0.849	4.206	0.177

Appendix C – Power and Temperature Experiment Data

T_sat [°C]	Tilt Angle [°]	Ambient [°C]	Power Input [W]	Loss [W]	Start-up Power [W]	T_excess [°C]
20	90	19.50	3.0	0.0	3.0	0.36
30	90	20.71	5.1	2.5	2.6	0.42
40	90	18.77	8.1	5.6	2.5	0.61
50	90	19.83	11.0	7.8	3.2	0.68
60	90	18.63	14.1	10.9	3.2	0.71
20	80	18.86	3.0	0.4	2.6	0.42
30	80	18.82	6.1	3.0	3.1	0.47
40	80	18.57	8.1	5.6	2.5	0.48
50	80	18.22	11.1	8.2	2.8	0.64
60	80	18.34	14.0	10.9	3.1	0.79
20	70	18.15	3.0	0.6	2.4	0.3
30	70	18.20	5.1	3.1	1.9	0.34
40	70	17.50	9.0	5.8	3.2	0.46
50	70	17.52	11.0	8.3	2.7	0.62
60	70	18.35	13.1	10.9	2.2	0.83
20	60	18.96	4.0	0.4	3.6	0.13
30	60	19.01	6.1	3.0	3.1	0.3
40	60	13.39	10.0	6.8	3.2	0.36
50	60	20.48	10.0	7.6	2.5	0.4
60	60	19.06	14.0	10.7	3.3	0.59

Appendix D – Thermal Conductivity vs. Tilt Angle Data

Tilt Angle [°]	T_evaporator [°C]	T_condenser [°C]	T_adiabatic [°C]	T_ambient [°C]	Heat Loss [W]	Q_in [W]	k [W/mK]
0	24.70	22.99	23.90	22.48	0.58	203	4942
10	24.45	22.81	23.38	22.54	0.50	203	5165
20	24.46	22.80	23.33	22.67	0.47	203	5119
30	24.40	22.80	23.31	22.61	0.47	203	5296
40	24.31	22.82	23.29	22.70	0.42	203	5653
50	24.21	22.81	23.23	22.65	0.41	203	6038
60	24.13	22.87	23.21	22.80	0.35	203	6729
70	24.10	22.94	23.19	23.10	0.26	203	7308
80	23.97	22.99	23.10	23.05	0.24	203	8622
90	24.00	23.06	23.25	22.96	0.27	203	8945